Icarus 229 (2014) 71–91

Contents lists available at ScienceDirect

Icarus

journal homepage: www.elsevier.com/locate/icarus

Numerical simulations of Jupiter's moist convection layer: Structure and dynamics in statistically steady states

K. Sugiyama [a,e,*], K. Nakajima [b], M. Odaka [c], K. Kuramoto [c,e], Y.-Y. Hayashi [d,e]

[a] Institute of Low Temperature Science, Hokkaido University, Sapporo 060-0819, Japan
[b] Department of Earth and Planetary Sciences, Kyushu University, Fukuoka 812-8581, Japan
[c] Department of Cosmosciences, Hokkaido University, Sapporo 060-0810, Japan
[d] Department of Earth and Planetary Sciences, Kobe University, Kobe 657-8501, Japan
[e] Center for Planetary Science, Kobe University, Kobe 650-0047, Japan

ARTICLE INFO

Article history:
Received 21 March 2013
Revised 16 September 2013
Accepted 12 October 2013
Available online 24 October 2013

Keywords:
Jovian planets
Jupiter, atmosphere
Atmospheres, dynamics
Atmospheres, structure

ABSTRACT

A series of long-term numerical simulations of moist convection in Jupiter's atmosphere is performed in order to investigate the idealized characteristics of the vertical structure of multi-composition clouds and the convective motions associated with them, varying the deep abundances of condensable gases and the autoconversion time scale, the latter being one of the most questionable parameters in cloud microphysical parameterization. The simulations are conducted using a two-dimensional cloud resolving model that explicitly represents the convective motion and microphysics of the three cloud components, H_2O, NH_3, and NH_4SH imposing a body cooling that substitutes the net radiative cooling. The results are qualitatively similar to those reported in Sugiyama et al. (Sugiyama, K. et al. [2011]. Intermittent cumulonimbus activity breaking the three-layer cloud structure of Jupiter. Geophys. Res. Lett. 38, L13201. doi:10.1029/2011GL047878): stable layers associated with condensation and chemical reaction act as effective dynamical and compositional boundaries, intense cumulonimbus clouds develop with distinct temporal intermittency, and the active transport associated with these clouds results in the establishment of mean vertical profiles of condensates and condensable gases that are distinctly different from the hitherto accepted three-layered structure (e.g., Atreya, S.K., Romani, P.N. [1985]. Photochemistry and clouds of Jupiter, Saturn and Uranus. In: Recent Advances in Planetary Meteorology. Cambridge Univ. Press, London, pp. 17–68). Our results also demonstrate that the period of intermittent cloud activity is roughly proportional to the deep abundance of H_2O gas. The autoconversion time scale does not strongly affect the results, except for the vertical profiles of the condensates. Changing the autoconversion time scale by a factor of 100 changes the intermittency period by a factor of less than two, although it causes a dramatic increase in the amount of condensates in the upper troposphere.

The moist convection layer becomes potentially unstable with respect to an air parcel rising from below the H_2O lifting condensation level (LCL) well before the development of cumulonimbus clouds. The instability accumulates until an appropriate trigger is provided by the H_2O condensate that falls down through the H_2O LCL; the H_2O condensate drives a downward flow below the H_2O LCL as a result of the latent cooling associated with the re-evaporation of the condensate, and the returning updrafts carry moist air from below to the moist convection layer. Active cloud development is terminated when the instability is completely exhausted. The period of intermittency is roughly equal to the time obtained by dividing the mean temperature increase, which is caused by active cumulonimbus development, by the body cooling rate.

1. Introduction

It is now an established fact that convective clouds are common entities in Jupiter's atmosphere (Vasavada and Showman, 2005). For example, Galileo and Cassini observed a number of small (~500–2000 km) convective clouds near the locations of lightning strikes (Little et al., 1999; Gierasch et al., 2000; Dyudina et al., 2004). Convective clouds are considered to play an important role

* Corresponding author. Present address: Institute of Space and Astronautical Science, JAXA, Sagamihara 252-5210, Japan.
E-mail address: sugiyama@gfd-dennou.org (K. Sugiyama).

0019-1035
http://dx.doi.org/10.1016/j.icarus.2013.10.016

in transferring heat from the interior of the planet to the upper troposphere (Gierasch et al., 2000). In due course, the mean vertical structure in the moist convection layer of Jupiter's atmosphere is thought to be maintained by the statistical contribution of a large number of clouds driven by internal and radiative heating/cooling over multiple cloud life cycles.

The mean vertical structure, i.e., the mean vertical profiles of temperature, condensates, and condensable gases, in the moist convection layer has been estimated using one-dimensional equilibrium cloud condensation models (ECCMs), where the profiles are derived from the thermodynamic equilibrium values of an adiabatically ascending air parcel from the deep atmosphere (Weidenschilling and Lewis, 1973; Atreya and Romani, 1985; Sugiyama et al., 2006). However, the results obtained by ECCMs should not be accepted without caution because they have neglected the effects of fluid dynamical and cloud microphysical processes associated with various atmospheric disturbances including convective clouds.

Although numerous attempts have been made to determine the vertical structure of Jupiter's atmosphere, many of the important properties of convective clouds are far from being constrained (reviewed by, e.g., West et al., 1986; Atreya et al., 1999; Vasavada and Showman, 2005), since the thick cloud deck prevents the vertical structure of the moist convection layer from being observed by remote sensing. Examples are the mean profiles of condensates and condensable gases; the Galileo probe is the first, and so far the only, spacecraft that carried out an in situ observation of the vertical structure of Jupiter's atmosphere from the level of visible clouds to approximately 20 bars. The results show an unexpectedly small amount of water vapor (Wong et al., 2004). However, the representativeness of the observed vertical structure is considered poor since the Galileo probe's entry site was one of the 5-μm hot spots which are atypical cloud-free regions in Jupiter's atmosphere. The mean atmospheric structure and its relationship to moist convection still remain unclear.

In order to investigate the possible structure and dynamics of the moist convection layer maintained by the statistical contribution of a large number of clouds over multiple cloud life cycles, numerical simulations using a cloud resolving model with long-term integration periods are indispensable. Such attempts have been rather rare, since most studies using cloud resolving models have focused on the evolution of a single cloud, in which the onset and initial expanding phase of a single cloud are considered under simplified and arbitrary initial conditions with short-term integration periods (e.g., Yair et al., 1992, 1995; Hueso and Sanchez-Lavega, 2001).

The purpose of our studies (Nakajima et al., 2000; Sugiyama et al., 2009, 2011) has been to investigate idealized mean profiles of condensable gases and condensates, which were formerly investigated by the use of ECCMs, and the temporal-spatial characteristics of convective motions that produce such profiles. For this purpose, we have been developing a two-dimensional cloud resolving model and performing long-term numerical simulations. The atmospheric structure obtained by Nakajima et al. (2000) is characterized by a thin but strong stable layer near the H_2O lifting condensation level that acts as a barrier for vertical convective motions, which is caused mainly by the change of mean molecular weight of atmospheric gases. This study suffered from two major limitations in that it considered only H_2O as a condensable component and employed unrealistically intense body cooling as a substitute for radiative cooling. Sugiyama et al. (2009) included, in addition to the condensation of H_2O, the condensation of NH_3 and the production reaction of NH_4SH, and Sugiyama et al. (2011) investigated the possible structure and dynamics of the moist convection layer using a body cooling whose cooling rate was of the order of that expected in Jupiter's atmosphere. The results suggested that the activity of moist convection is not steady but experiences a prominent quasi-periodic variation with a period of several tens of days. Around the levels where NH_3 condensation and NH_4SH chemical reaction occur, weak but definite stable layers develop and act as dynamical and compositional boundaries during the period of weak convective activity.

Although Sugiyama et al. (2011) succeeded in obtaining an insightful image of the structure and dynamics of the moist convection layer in Jupiter's atmosphere, the dependence of the structure and dynamics on parameters that are poorly constrained by observations remains to be examined. One of the most important parameters to be considered is the deep abundances of condensable gases. Not only the altitudes at which condensation and chemical reaction occur but also dynamical properties should be affected by this parameter, since the vertical profile of static stability is governed by the deep abundances of condensable gases (Sugiyama et al., 2006). The deep abundance of H_2O gas is the most ambiguous. The Galileo probe could not provide a confident estimate (Wong et al., 2004), and indirect evidence suggests that the deep abundance of H_2O gas is higher than the solar abundance (Atreya et al., 1999). We therefore perform a parameter experiment on the deep abundances of condensable gases.

Also poorly constrained are details of cloud microphysical processes. There have been some attempts (e.g., Rossow, 1978; Carlson et al., 1988) to estimate the time scales involved in such processes. Gibbard et al. (1994) and Yair et al. (1998) also considered cloud microphysical processes in order to investigate lightning in Jupiter's convective clouds observed by spacecraft, and succeeded in demonstrating its existence. However, there have been no quantitative measurements of the amount, size, type, and composition of cloud particles, to which the representation of cloud microphysics in numerical models can be compared. Thus, we hesitate to use a highly sophisticated bulk microphysical parameterization scheme such as that implemented in the EPIC model (Palotai and Dowling, 2008). Instead, we implement a simple bulk parameterization scheme, as will be fully described in Section 2, and perform a parameter experiment on the autoconversion time scale. The reason we chose the autoconversion time scale as the parameter to be varied is that it is the most ambiguous parameter of all those controlling the rate of condensate removal from an air parcel. For instance, at least for the case of Earth-like conditions, Nakajima and Matsuno (1988) showed by the use of long-term numerical calculations that switching off the autoconversion process destroys the asymmetry between narrow, strong, cloudy updrafts and wide, weak, dry downdrafts, which is a distinct characteristic of the troposphere of Earth, and produces a troposphere completely filled with condensate. Switching on/off other processes such as evaporation of precipitating condensate and negative buoyancy of condensate does not result in such an extreme change.

In this study, a number of long-term numerical simulations are performed in order to examine the dependence of the idealized structure and dynamics of the moist convection layer in statistically steady states on the autoconversion time scale and on the deep abundances of condensable gases. We also examine the mechanism of the most significant characteristic, the intermittent emergence of vigorous cumulonimbus clouds, obtained in most of our calculations. In Section 2, we present a brief description of our cloud resolving model and the settings for the parameter experiments. In Section 3, we summarize the characteristics of the structure and dynamics of the moist convection layer obtained by a control experiment in which the settings are identical to those of Sugiyama et al. (2011). In Sections 4 and 5, we demonstrate the dependences of the structure and dynamics of the moist convection layer on the autoconversion time scale and on the deep abundances of condensable gases, respectively. We discuss the

mechanism that causes intermittent cloud activity in Section 6, and provide concluding remarks in Section 7.

2. Numerical model and settings of parameter experiments

The framework of our numerical model and the experimental settings we adopt are chosen as simple ones that can mimic Jupiter's atmosphere, which is maintained by the balance among the upwelling heat flux from the deep interior, the upward heat transport by moist convection, and net radiative cooling caused by solar and long-wave radiation. The effect of the heat supply from the deep interior is realized by keeping the values of the potential temperature and mixing ratios constant at the lower boundary. By doing so, we assume the region below the lower boundary to be a huge reservoir, in which heat and condensable gases are transported upward and well mixed by convection in the deep atmosphere. The net radiative cooling is simply represented as horizontally and temporally uniform body cooling at the upper troposphere, instead of being calculated by the use of a radiative transfer model. We suppose that the assumption of temporally and horizontally uniform cooling is acceptable at least as the first step of consideration of statistically steady states.

Numerical experiments are conducted for periods much longer than the lifetime of individual cumulonimbus clouds, because the purpose of the experiments is to realize the possible structure and dynamics of the moist convection layer established as statistically steady states by the interaction among the internal heating from the deep interior, the moist convection, and net radiative cooling. During the course of long-term integration of the numerical model, the initially given vertical profiles of temperature and mixing ratios of the condensable gases are forgotten, and the mean atmospheric profiles gradually evolve to be those governed by the internal processes in the model, which are the states of the atmosphere with which we are concerned in this study. In this respect, the numerical experiments in the present study are distinctly different from those for the simulation of a single cloud (e.g., Yair et al., 1992, 1995; Hueso and Sanchez-Lavega, 2001), where the profiles of temperature and mixing ratios are important control parameters. In contrast, these profiles are not control parameters but part of the results of our calculations.

2.1. Numerical model

Here we briefly describe the cloud resolving model utilized in this study. A more complete description can be found in Sugiyama et al. (2009). Our model is available at http://www.gfd-dennou.org/library/deepconv/.

The dynamical framework of our model is two-dimensional in the horizontal and vertical directions, and is based on the quasi-compressible system (Klemp and Wilhelmson, 1978). In this framework, the variables are divided into a horizontally uniform basic state in hydrostatic equilibrium and residual perturbation, and prognostic equations of residual perturbations are solved.

Derivation of the momentum and pressure equations require use of an equation of state that includes the effects of condensable species.

$$\rho = \frac{p}{R_d T_v} = \frac{p}{R_d T}\left(\frac{1/M_d}{1/M_d + \sum q_v/M_v}\right)\left(1 + \sum q_v + \sum q_c\right), \tag{1}$$

where ρ is the density of moist air, p is the pressure, R_d is the gas constant for dry air per unit mass, T is the temperature, T_v is the virtual temperature, and M_d and M_v are the molecular weight of the non-condensable and condensable components, respectively. q_v is the mixing ratio of each condensable gas, q_c is the mixing ratio of each condensate, and $\sum$ indicates the summation regarding condensable gases or condensates. By using Eq. (1), the Exner function (non-dimensional pressure), π, is written in the form

$$\pi \equiv \left(\frac{p}{p^*}\right)^{R_d/c_{p_d}} = \left(\frac{R_d}{p^*}\rho\theta_v\right)^{R_d/c_{p_d}}, \tag{2}$$

where p^* is the reference pressure, c_{p_d} is the specific heat of dry air at constant pressure, and θ_v is the virtual potential temperature defined by

$$\theta_v \equiv \frac{\theta}{\left(\frac{1/M_d}{1/M_d + \sum q_v/M_v}\right)(1 + \sum q_v + \sum q_c)} \tag{3}$$

and the potential temperature θ is $\theta = T/\pi$. This dynamical framework ignores the dependence of the mean specific heat on the temperature and composition, since the potential temperature is utilized. However, the value of the static stability N^2, which governs the overall structure of the moist convection layer, is almost the same as that obtained when the dependences ignored above are taken into consideration (Sugiyama et al., 2009).

The momentum equations are expressed in the following forms,

$$\frac{\partial u}{\partial t} = -\left(u\frac{\partial u}{\partial x} + w\frac{\partial u}{\partial z}\right) - c_{p_d}\theta_{v0}\frac{\partial \pi'}{\partial x} + Turb.u, \tag{4}$$

$$\frac{\partial w}{\partial t} = -\left(u\frac{\partial w}{\partial x} + w\frac{\partial w}{\partial z}\right) - c_{p_d}\theta_{v0}\frac{\partial \pi'}{\partial z} + \left(\frac{\theta'_v}{\theta_{v0}}\right)g + Turb.w, \tag{5}$$

where u is the velocity in the x direction, w is the velocity in the z direction, g is the acceleration due to gravity, and $Turb.u$ and $Turb.w$ refer to subgrid scale turbulent momentum mixing. The variables denoted by "0" and "′" represent a horizontally uniform basic state and residual perturbation, respectively, which satisfy the relation, e.g., $\theta = \theta' + \theta_0$ ($\theta' \ll \theta_0$). The buoyancy term in Eq. (5) can be rewritten as

$$\left(\frac{\theta'_v}{\theta_{v0}}\right)g = \left(\frac{\theta'}{\theta_0} + \frac{\sum(q'_v + q_{v0})/M_v}{1/M_d + \sum q_{v0}/M_v} - \frac{\sum(q'_v + q_{v0}) + \sum q'_c}{1 + \sum q_{v0}}\right)g. \tag{6}$$

Note that the mixing ratio of each condensate in the basic state is set to zero. The pressure equation is derived by using Eqs. (1)–(3), the compressible continuity equation

$$\frac{\partial \rho}{\partial t} + \frac{\partial}{\partial x_j}(\rho u_j) = 0,$$

and the thermodynamic equation (Eq. (8)), which will be described later,

$$\frac{\partial \pi'}{\partial t} = -\frac{{C_{s0}}^2}{c_{p_d}\rho_0\theta_{v0}^2}\frac{\partial}{\partial x_j}(\rho_0\theta_{v0}u_j), \tag{7}$$

where C_{s0} is the phase velocity of sound given by ${C_{s0}}^2 = c_{p_d}R_d\pi_0\theta_{v0}/c_{v_d}$, and c_{v_d} is the specific heat at constant volume. The terms that correspond to pressure variation caused by diabatic heating are neglected following Klemp and Wilhelmson (1978). The thermodynamic equation can be written as

$$\frac{\partial \theta'}{\partial t} = -\left(u\frac{\partial \theta'}{\partial x} + w\frac{\partial \theta'}{\partial z}\right) - w\frac{\partial \theta_0}{\partial x} + \frac{1}{\pi_0}(Q_{cnd} - Q_{rad} + Q_{dis}) + Turb.\theta, \tag{8}$$

where Q_{cnd} refers to heating by condensation and chemical reaction, Q_{rad} represents body cooling, and Q_{dis} and $Turb.\theta$ refer to dissipative heating and subgrid scale turbulent mixing of potential temperature, respectively. The conservation equation for each condensable gas or condensate can be written in the form

$$\frac{\partial q'}{\partial t} = -\left(u\frac{\partial q'}{\partial x} + w\frac{\partial q'}{\partial z}\right) - w\frac{\partial q_0}{\partial x} + Src.q + Turb.q, \quad (9)$$

where *Src.q* refers to source terms associated with the cloud microphysical parameterization and *Turb.q* refers to the subgrid scale turbulent mixing terms. Eq. (9) represents nine equations, i.e., the conservation equations for three condensable gases, three non-precipitating condensates, and three precipitating condensates, because we consider three condensable components in Jupiter's atmosphere and employ the bulk parameterization scheme of Kessler (1969) as mentioned below.

As a minimal model that can represent the most essential processes of cloud microphysics, we use a bulk parameterization scheme based on Kessler (1969), which has been used in modeling studies on terrestrial moist convection. In the scheme, each condensate is simply divided into two categories, "non-precipitating condensate" and "precipitating condensate." Although it is unclear how well the scheme represents the actual cloud microphysical processes in Jupiter's atmosphere, Yair et al. (1992) uses the scheme as the first step in considering moist convection, and Hueso and Sanchez-Lavega (2001) uses a very similar scheme. As mentioned in Sugiyama et al. (2009), some of the parameters in Kessler's parameterization used in our model are modified from the original ones for Earth's atmosphere following Nakajima et al. (2000). The growth rate of precipitating condensates by collecting non-precipitating condensates and the terminal velocity for precipitating condensates are increased by a factor of 3, considering the terminal velocity of condensate particles calculated by Yair et al. (1995). In addition, autoconversion from non-precipitating to precipitating condensates is accelerated by 10 times considering the results of Rossow (1978) and Carlson et al. (1988), in which precipitation-size particles are expected to form rapidly in Jupiter's atmosphere.

We do not try to implement possible categories of condensates. In the case of Earth's clouds, highly sophisticated bulk microphysical parameterization schemes have been developed. Some of them treat liquid and solid phases separately, distinguish several categories of icy particles, i.e., ice crystals, snowflakes, graupel, and hail, and estimate the interactions among them (Straka, 2009). Naturally, we cannot use those schemes because their performance in Jupiter's atmosphere is not at all guaranteed. Not only the interaction among the categories but also the specifications of the categories themselves strongly depend on observational and experimental facts collected exclusively for Earth's clouds. Furthermore, the microphysical behavior of NH_3 and NH_4SH particles is completely unknown. Considering the currently available knowledge about the microphysics of Jupiter's clouds, we think that the use of the Kessler type scheme with minimal complexity is reasonable for the time being. Improvement of the microphysical scheme is important, but is a future issue.

We simplify the radiative process, instead of calculating it by the use of a radiative transfer model. The model atmosphere is subject to an externally given body cooling that is a substitute for radiative cooling, as mentioned in the first paragraph of Section 2. The subgrid scale turbulence parameterization scheme of 1.5-order closure (Klemp and Wilhelmson, 1978) is implemented, where turbulent mixing coefficients are diagnosed from turbulent kinetic energy that is predicted by a prognostic equation.

2.2. Experimental settings

The experimental settings are schematically shown in Fig. 1. The computational domain covers the region of 300 km in the vertical direction (from 30 bar to 0.001 bar) and 1024 km in the horizontal direction. The spatial resolution is 2 km in both the horizontal and the vertical directions. The cyclic boundary condition is applied in the horizontal direction. The conditions of free-slip and vanishing vertical velocity are applied at the upper and lower boundaries. Hereafter, as shown in Fig. 1, "dry convection layer," "moist convection layer," and "tropopause" are defined as the region from the lower boundary to the H_2O lifting condensation level, the region from the H_2O lifting condensation level to $p = 0.1$ bar, and the level at $p = 0.1$ bar, respectively.

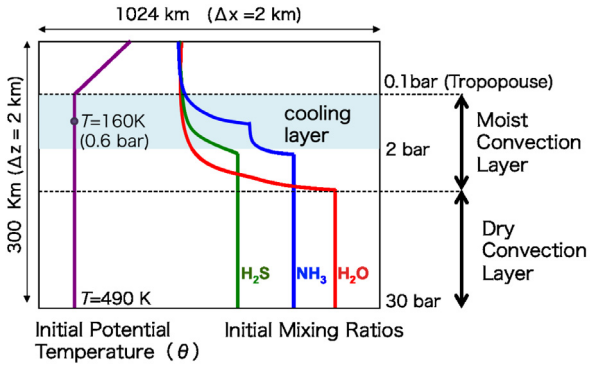

Fig. 1. Schematic view of experimental settings.

The model atmosphere consists of H_2, He, H_2O, NH_3, and H_2S. H_2 and He are treated as dry (non-condensable) components while H_2O, NH_3, and H_2S are treated as condensable components. Solid H_2O, solid NH_3, and solid NH_4SH are treated as condensates. The acceleration of gravity is set to 23.1 m/s. The values of potential temperature and mixing ratios of the condensable gases at the lower boundary are kept constant in order to represent the effect of convection in the deeper planetary interior implicitly, as mentioned in the first paragraph of Section 2.

The initial mixing ratio of each condensable gas is equal to that given at the lower boundary below the pressure level where condensation or chemical reaction of NH_4SH formation occurs. Above these levels, all mixing ratios are set to be slightly below their saturated values. The initial temperature profile from the lower boundary to $p = 0.1$ bar level is dry adiabatic, i.e., constant potential temperature, that passes through 490 K at the lower boundary and 160 K at 0.6 bar, and is isothermal above 0.1 bar. At the initial time, the model atmosphere is motionless. In order to seed a convective motion, a small random potential temperature perturbation is added to the grid points near the H_2O lifting condensation level.

2.3. Experimental parameters

The experimental parameters in our calculations are listed in Table 1. The autoconversion time scale, τ_{auto}, is varied. The conversion

Table 1
Experimental parameters.

Run	Body cooling rate (K/day)	Abundances at the lower boundary (solar)	Autoconversion time scale (s)
CTRL[a]	0.01	1.0	100
C10	0.01	1.0	1000
C100	0.01	1.0	10,000
R10S01	0.1	0.1	100
R10	0.1	1.0	100
R10S3	0.1	3.0	100
R10S10	0.1	10.0	100
R3[b]	0.3	1.0	100
R100[c,b]	1.0	1.0	100

[a] The settings for CTRL are identical to those of Sugiyama et al. (2011).
[b] The results are only shown in Appendix A.
[c] The settings for R100 are identical to those of Sugiyama et al. (2009), except for a change in the horizontal domain from 512 km to 1024 km.

rate from non-precipitating to precipitating condensate due to the autoconversion process, *CN*, is expressed as

$$CN = (q'_{c1} - q^0)/\tau_{\rm auto},$$

where q'_{c1} and q^0 are the mixing ratio of each non-precipitating condensate and the threshold mixing ratio of each condensate, respectively. In the control experiment, the value of $\tau_{\rm auto}$ is set to 100 s, which is an order of magnitude shorter than the standard value used for Earth's atmosphere as is noted in Section 2.1, and the value of q^0 is set to zero. The reason for adopting $q^0 = 0$ is that we have simply no clue as to choice of its value. We perform additional numerical calculations with larger values of $\tau_{\rm auto}$. The longest time scale employed, 10,000 s, is selected in order to satisfy the condition that the value of $\tau_{\rm auto}$ is longer than the time scale of vertical advection in the moist convection layer.

The abundance of each condensable gas at the lower boundary is varied from 0.1 to 10 times solar. As for the solar abundance, mixing ratios of H_2O, NH_3, and H_2S are 6.1×10^{-3}, 7.6×10^{-4}, and 3.5×10^{-4} kg/kg, respectively (Grevesse et al., 2007).

The body cooling rate is also varied. The cooling rate for the control experiment is 0.01 K per terrestrial day, which is reasonably compatible with the cooling rate determined by the Galileo probe (Sromovsky et al., 1998), and the total energy loss $\sim$11.4 W/m^2 by cooling is also compatible with the globally averaged thermal emission (Hanel et al., 1981). However, it should be noted that, in the parameter experiment on the deep abundances of condensable gases, the specified body cooling rate is set to 0.1 K rather than 0.01 K per terrestrial day in order to reduce the CPU time required to achieve a statistical steady state in the model atmosphere. The dependence of the structure and dynamics of the moist convection layer on the body cooling rate is summarized in Appendix A. The structure and dynamics of the moist convection layer obtained in a calculation using a large amount of body cooling share several qualitative features with those in the control experiment, as will be shown later.

3. The structure and dynamics of the moist convection layer obtained in the control experiment

The CTRL listed in Table 1, whose settings are identical to those of Sugiyama et al. (2011), is chosen as the control experiment in our study. In this section, we describe key aspects of CTRL referring to the figures showing the thermal and the vertical velocity structures, which are not presented in detail in Sugiyama et al. (2011). In the following, the lifting condensation level (LCL) of each condensable gas is defined as the condensation or chemical reaction level obtained by an ECCM using the thermodynamic subroutine in the cloud resolving model, in which a thermally equilibrium air parcel adiabatically ascends from the lower boundary. The LCLs of H_2O, NH_4SH, and NH_3 are about 4.0 bar, 1.7 bar, and 0.5 bar, respectively.

3.1. Temporal variation of the structure and dynamics of the moist convection layer

The results of CTRL are characterized by a quasi-periodic emergence of vigorous deep clouds rising from the H_2O LCL to the tropopause. Hereafter, the vigorous deep clouds are referred to as "cumulonimbus clouds," and the periods of strong cumulonimbus activity are referred to as "active periods," whereas the periods between consecutive active periods are referred to as "quiet periods."

Fig. 2(a) shows a typical cycle of the horizontal-mean mixing ratios of the condensates. The durations of the active periods, marked as "A," are only 1–2 days, while that for the quiet period, marked as "Q," is considerably longer. At the beginning of the quiet period, only NH_3 clouds develop. Then, NH_4SH clouds appear, followed by H_2O clouds. The base of H_2O cloud gradually descends with time. Eventually, the quiet period ends with the explosive development of cumulonimbus clouds. The quasi-periodicity of this active-quiet cycle was exemplified in Fig. 1 and Animation 1 of Sugiyama et al. (2011) and will be shown later in Fig. 6(a1). The mean period

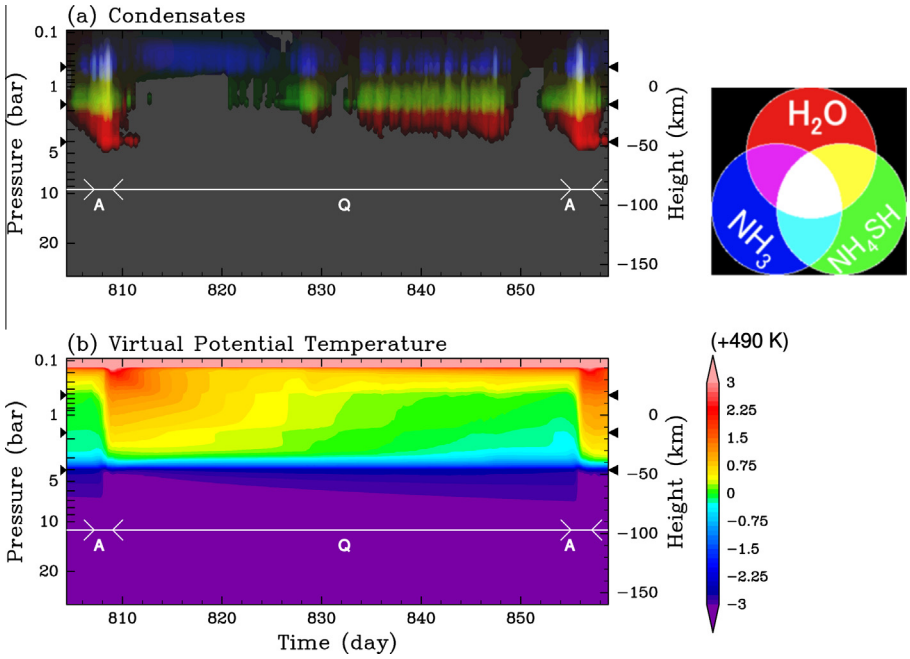

Fig. 2. Temporal variation of (a) horizontal mean mixing ratios of condensates and (b) horizontal mean virtual potential temperature obtained in CTRL. In (a), H_2O condensate, NH_4SH condensate, and NH_3 condensate are indicated by red, green, and blue color tones, respectively. Tone intensity represents mixing ratio (kg/kg) on a logarithmic scale ranging from 1.0×10^{-8} to 1.0×10^{-4} kg/kg. Multiple composition clouds are represented by a mixture of the three colors. Black triangles on the left and the right edges of each panel indicate the NH_3, NH_4SH, and H_2O LCLs from top to bottom. Active periods and quiet periods are marked as "A" and "Q," respectively. Altitude is measured from the level of 1 bar. (For interpretation of the references to color in this figure legend, the reader is referred to the web version of this article.)

of intermittency averaged over the last 4 active-quiet cycles is about 41 days.

Fig. 2(b) shows a typical cycle of virtual potential temperature, θ_v, in the same time span shown in Fig. 2(a). The definition of θ_v is as given in Eq. (3). In Fig. 2(b), a variation of θ_v synchronized with the intermittent cloud activity is clearly seen in the moist convection layer; the value of θ_v rapidly increases during the active periods, and decreases steadily with time during the quiet period. The variation of θ_v arises, since condensation heating in the moist convection layer is concentrated almost exclusively during the active periods. The temporal variation of θ_v at a pressure level is sawtooth-like, as will be shown later in Fig. 6(a2).

Fig. 3(a–c) shows snapshots of a selected set of variables during the quiet period shown in Fig. 2. At the beginning of this quiet period (Fig. 3(a)), moist convection associated with NH_3 condensation occurs and the NH_3 clouds are distributed horizontally. Vertical motion is present not only above the NH_3 LCL but also below this LCL, since evaporation of precipitating NH_3 condensate drives downdrafts below the NH_3 LCL. The peak velocities of the updrafts and downdrafts found near the tropopause are about 3 m/s and −3 m/s, respectively. The vertical motion below the H_2O LCL is the remnant of convective motion driven during the previous active period. As time progresses, NH_4SH clouds develop (Fig. 3(b)). Below each of the updrafts associated with NH_4SH condensation, a downdraft is driven by the evaporation of precipitating NH_4SH condensate. Following the onset of NH_4SH clouds, H_2O clouds begin to form locally (Fig. 3(c)) in the updrafts that develop as the returning flows associated with downward plumes driven by the evaporation of precipitating NH_4SH condensate. Mixing of different condensable gases and condensates across the NH_3 LCL or NH_4SH LCL is weak, but occurs occasionally due to the upward or downward penetration of convective plumes. The peak velocities of the updrafts and downdrafts in the moist convection layer are about 10 m/s and −10 m/s, respectively.

Fig. 3(d) shows snapshots of the active period that occurs after the quiet period shown in Fig. 3(a–c). The vertical motion in the moist convection layer is characterized by narrow, strong, cloudy updrafts and wide, weak, dry downdrafts. The maximum mixing ratio of H_2O condensate is about 4.0×10^{-3} kg/kg. The peak velocities of the updrafts and the downdrafts in the moist convection layer are about 50 m/s and −10 m/s, respectively. The updrafts during the active period are about five times as strong as those in the quiet period (Fig. 3(b) and (c)). In the dry convection layer, strong downdrafts (~ -50 m/s) are found just beneath cumulonimbus clouds, which are driven by the latent cooling caused by the re-evaporation of H_2O condensate. Fig. 3(d) also shows that the vigorous vertical transport associated with the convective circulation during the active periods strongly modifies the distributions of condensable gases and condensates from those expected by the ECCM. Considerable amounts of H_2O and NH_4SH condensates are transported upward from their respective LCLs to the tropopause as indicated by the white color region in Fig. 3(d1). The distribution of each condensable gas mixing ratio is highly inhomogeneous in the horizontal direction (Fig. 3(d2)). Even below the H_2O LCL, a slight inhomogeneity of mixing ratios of condensable gases associated with the downdrafts is found.

During the quiet period in Fig. 3(b6) and (c6), the vertical profiles of the intensity of vertical motion as represented by root mean square of the vertical velocity, $\sqrt{\overline{w^2}}$, have either a local minimum or inflection points at the NH_3 and the NH_4SH LCLs. Corresponding to these vertical profiles, a staircase-like structure of the horizontal mean mixing ratio of NH_3 gas develops (Fig. 3(b5) and (c5)); its vertical gradient is intensified at the NH_4SH LCL and the NH_3 LCL, whereas the mean mixing ratio becomes more uniform between the two LCLs resulting from the mixing caused by the vertical motions. These features could be regarded as the manifestation of a dynamical and compositional boundary resulting from the enhancement of static stability at the LCLs (e.g., Sugiyama et al., 2006).

During the active period, the NH_3 and NH_4SH LCLs act neither as dynamical nor compositional boundaries; not only the intense updrafts in the vigorous cumulonimbus clouds but also the dry downdrafts penetrate these two LCLs (Fig. 3(d3)). However, the H_2O LCL continues to act as a significant dynamical and compositional boundary implied by both $w \sim 0$ and the local minimum of $\sqrt{\overline{w^2}}$ at the H_2O LCL (Fig. 3(d3) and (d6)).

Fig. 4(a) shows the temporal variations of vertically integrated heating due to condensation, advection, body cooling, subgrid turbulence, and the heat flux at the lower boundary in the moist convection layer and dry convection layer during the quiet periods. Fig. 4(b) is the same as Fig. 4(a) but for the active periods. In the moist convection layer, the condensation heating associated with the cumulonimbus clouds is dominant during the active period, while the body cooling is dominant during the quiet period. The maximum rate of condensation heating in the active period is about 100 times larger than that of the body cooling. The intense condensation heating during the active period is caused by the successive formation of vigorous cumulonimbus clouds in a short time, as shown in Figs. 2 and 3(d).

In the dry convection layer, significant heating occurs only during the active period (Fig. 4(a) and (b)). During the active period, latent cooling due to the evaporation of precipitating H_2O condensate from cumulonimbus clouds drives vertical motion. The downward advected cold air parcels cool the region near the lower boundary. The cooling near the lower boundary is balanced by the heat flux from the lower boundary, where the potential temperature is kept constant.

3.2. Time and horizontal mean structure of the moist convection layer

Fig. 5(a) shows the horizontal mean profiles of the mixing ratios of the condensates averaged over the last 4 active-quiet cycles. The vertical profiles averaged only over the active periods and those only over the quiet periods are also shown by broken and dashed lines, respectively. Two distinct features can be observed in the mean vertical profiles. First, all of the condensates are advected upward to significant heights; H_2O and NH_4SH particles are advected up to altitudes above the NH_3 LCL. Second, the maximum values for mixing ratios of all of the condensates are fairly close to each other; they are approximately $1.0 - 2.0 \times 10^{-6}$ kg/kg. The mean mixing ratio of a condensate, $\bar{q}_c'$, can be estimated using that averaged only over the active periods, $\bar{q}_c'^a$, typical length of the active period, Δt^a, and the mean period of intermittency, Δt, as $\bar{q}_c' = \bar{q}_c'^a \Delta t^a / \Delta t$, since the contributions during the quiet periods are negligible.

Fig. 5(b) shows the vertical profiles of horizontal mean mixing ratios of condensable gases averaged over the last 4 active-quiet cycles. Also shown are the corresponding vertical profiles obtained by the ECCM. The profiles of the condensable gases in the cloud resolving model exhibit quite different characteristics from those obtained by the ECCM. In the cloud resolving model, each condensable gas is significantly undersaturated in the moist convection layer and mixing ratios of NH_3 and H_2S gases begin to decrease with height not at their respective LCLs, but at the H_2O LCL. These features are one of the manifestations of vigorous vertical mixing of dry and condensable gases caused by the intense convective circulation during the active periods.

Fig. 5(c) shows the horizontal mean vertical profiles of static stability N^2 (the square of buoyancy frequency, N). There is a distinct maximum of N^2 at the H_2O LCL, which explains the reason that the level acts as a both dynamical and compositional boundary even during the active periods shown in Fig. 3(d). Weaker peaks are also present at the NH_3 and NH_4SH LCLs. The reason

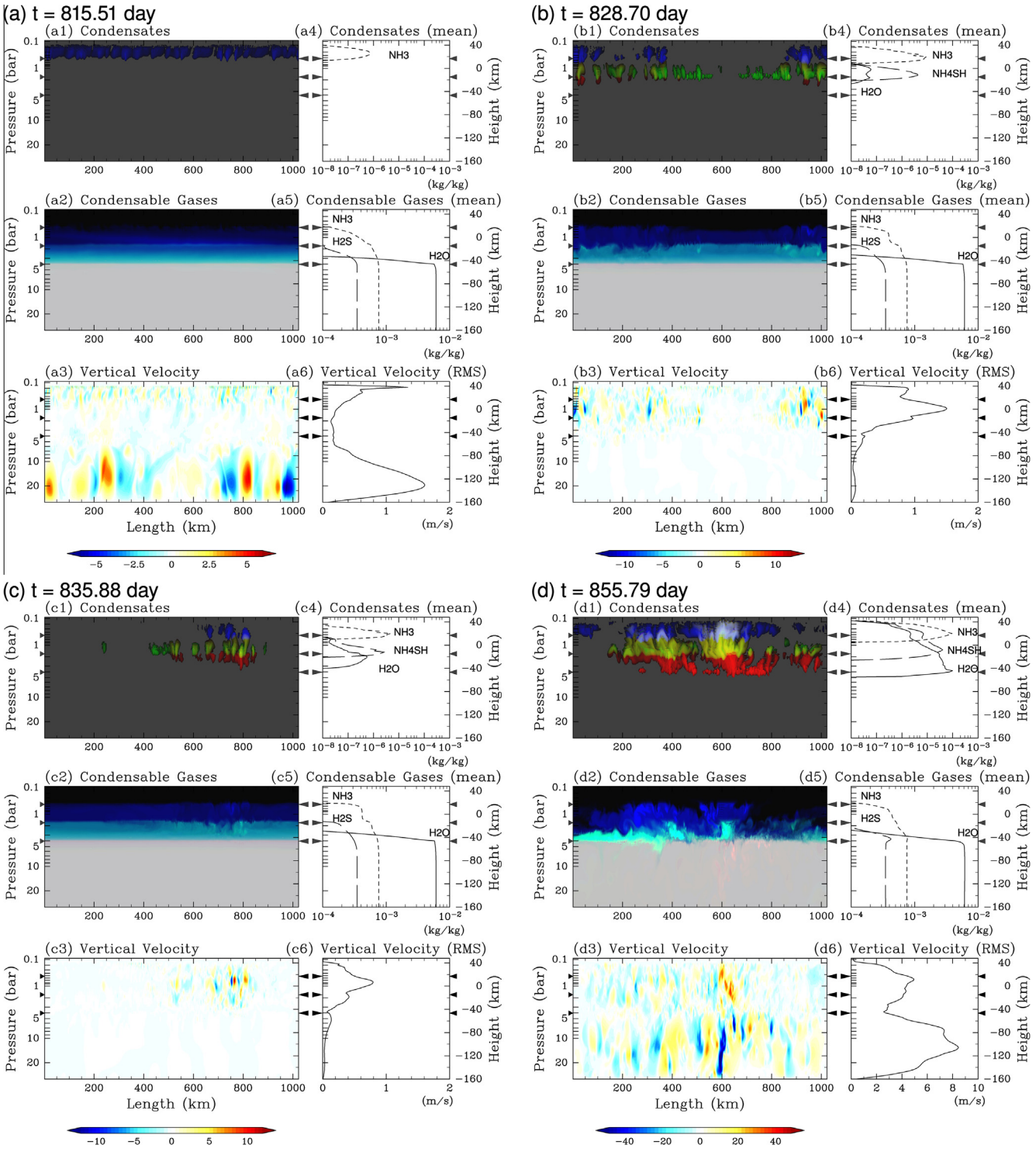

Fig. 3. Temporal evolution of convection obtained in CTRL. (a) Snapshots at $t = 815.51$ day in a quiet period. (a1) Mixing ratios of condensates plotted in the same manner as in Fig. 2 but with a different logarithmic scale ranging from 1.0×10^{-8} to 1.0×10^{-3} kg/kg for each condensate. (a2) Mixing ratios of condensable gases plotted indicating H_2O, H_2S, and NH_3 gases by red, green, and blue color tones, respectively. Tone intensity represents mixing ratio (kg/kg) on a linear scale normalized by the corresponding initial value. (a3) Vertical velocity. (a4) Horizontal mean mixing ratios of condensates. Solid, broken, and dashed lines indicate H_2O, NH_4SH, and NH_3 condensates, respectively. (a5) Horizontal mean mixing ratios of condensable gases. Solid, broken, and dashed lines indicate H_2O, H_2S, and NH_3 gases, respectively. (a6) Root mean square (RMS) of the vertical velocity. (b) Same as (a) but for $t = 828.70$ day. (c) Same as (a) but for $t = 835.88$ day. (d) Same as (a) but for $t = 855.79$ day in a active period. Black triangles on the left and the right edges of each panel indicate the NH_3, NH_4SH, and H_2O LCLs from top to bottom. (For interpretation of the references to color in this figure legend, the reader is referred to the web version of this article.)

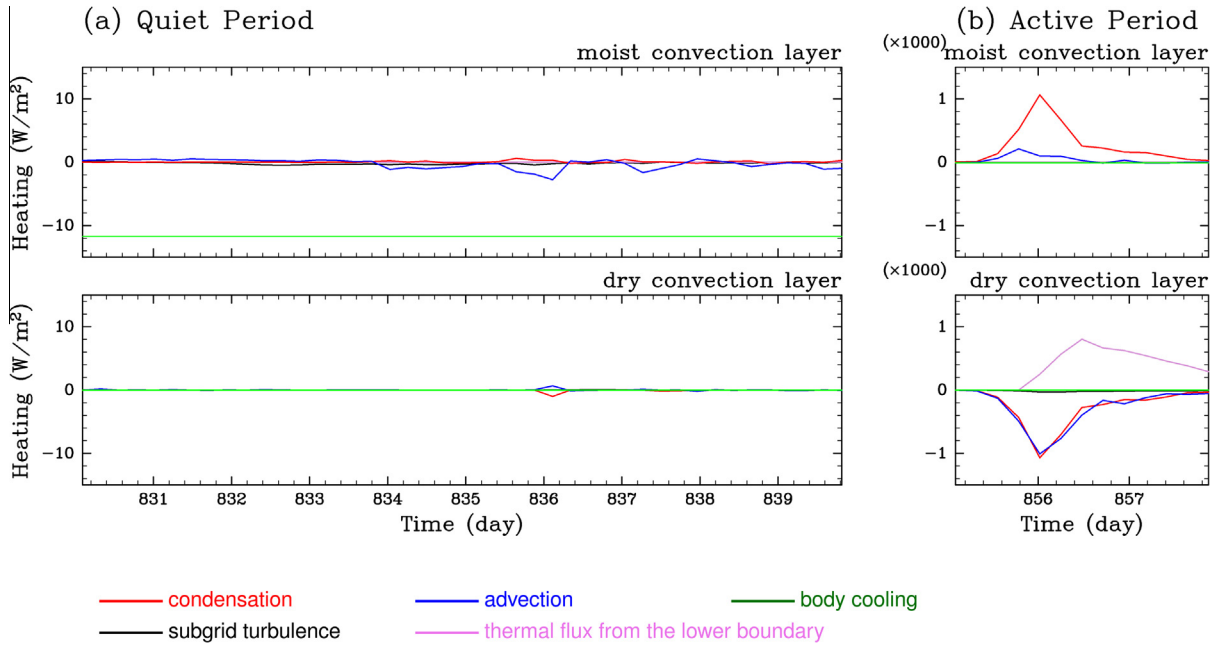

Fig. 4. Temporal variation of vertically integrated heating for (a) a quiet periods and (b) an active periods. Heating due to condensation, advection, body cooling, subgrid turbulence, and thermal flux from the lower boundary are indicated by red, blue, green, black, and violet lines, respectively. (For interpretation of the references to color in this figure legend, the reader is referred to the web version of this article.)

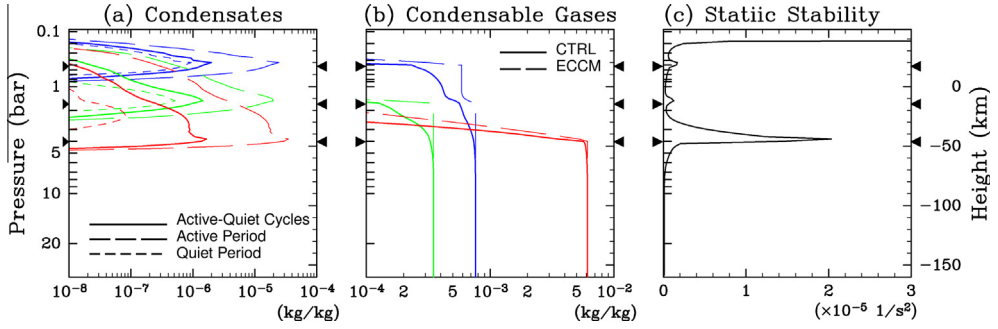

Fig. 5. (a) Vertical profiles of horizontal mean mixing ratios of condensates averaged over the last 4 active-quiet cycles. Blue, green, and red lines indicate NH_3, NH_4SH, and H_2O,respectively. Solid, broken, and dashed lines indicate the profiles averaged over the periods of the entire active-quiet cycles, those only over the active period, and those only over the quiet period, respectively. (b) Vertical profiles of horizontal mean mixing ratios of condensable gases. Blue, green, and red lines indicate NH_3, H_2S, and H_2O, respectively. Thin broken lines represent profiles obtained by the ECCM. (c) Static stability N^2. Black triangles on the left and the right edges of each panel indicate the NH_3, NH_4SH, and H_2O LCLs from top to bottom. (For interpretation of the references to color in this figure legend, the reader is referred to the web version of this article.)

for the formation of such stable layers is that condensation of these condensable gases not only releases latent heat energy but also reduces the mean molecular weight, since those gases are heavier than hydrogen, the dominant "dry" component of Jupiter. The H_2O LCL remains stable at all times, since the active periods begin before the atmosphere at the H_2O LCL becomes neutral or unstable due to the triggering effect caused by precipitating H_2O condensate as will be described in Section 6.

4. Dependence on the autoconversion time scale

In this section, the dependence of the structure and dynamics of the moist convection layer on the autoconversion time scale, τ_{auto}, is examined. The left panels of Fig. 6 show the temporal variations of the horizontal mean mixing ratios of the condensates and virtual potential temperature at $p = 2$ bar for CTRL, C10, and C100 listed in Table 1, where the values of τ_{auto} are 100 s, 1000 s, 10,000 s, respectively. The overall features of temporal variations of cloud activity and virtual potential temperature, namely the existence of the intermittency and sawtooth-like variation, do not seem to change greatly with the increase of τ_{auto}. However, there are modest quantitative differences among the three cases. For example, compared to the results of CTRL, the amplitude of temporal variation of virtual potential temperature is larger and the period of the intermittency observed is longer in C10 and C100. The mean periods of the intermittency in C10 and C100 averaged over the last 4 active-quiet cycles are about 54 and 61 days, 1.3 and 1.5 times that of CTRL, respectively.

The mean vertical profiles of the condensates, on the other hand, vary considerably with different values of τ_{auto} as is shown in the right panels of Fig. 6 for both the active and the quiet periods. There is a notable difference in the amount of condensates among these cases. Especially, considerable amounts of the NH_4SH and the H_2O condensates exist near the tropopause during the quiet periods in C100. Fig. 7(a–c) compares the vertical profiles of the horizontal mean mixing ratios of the condensates averaged over the last 4 active-quiet cycles. The mean vertical profiles observed in C100 are also very different to those observed in the

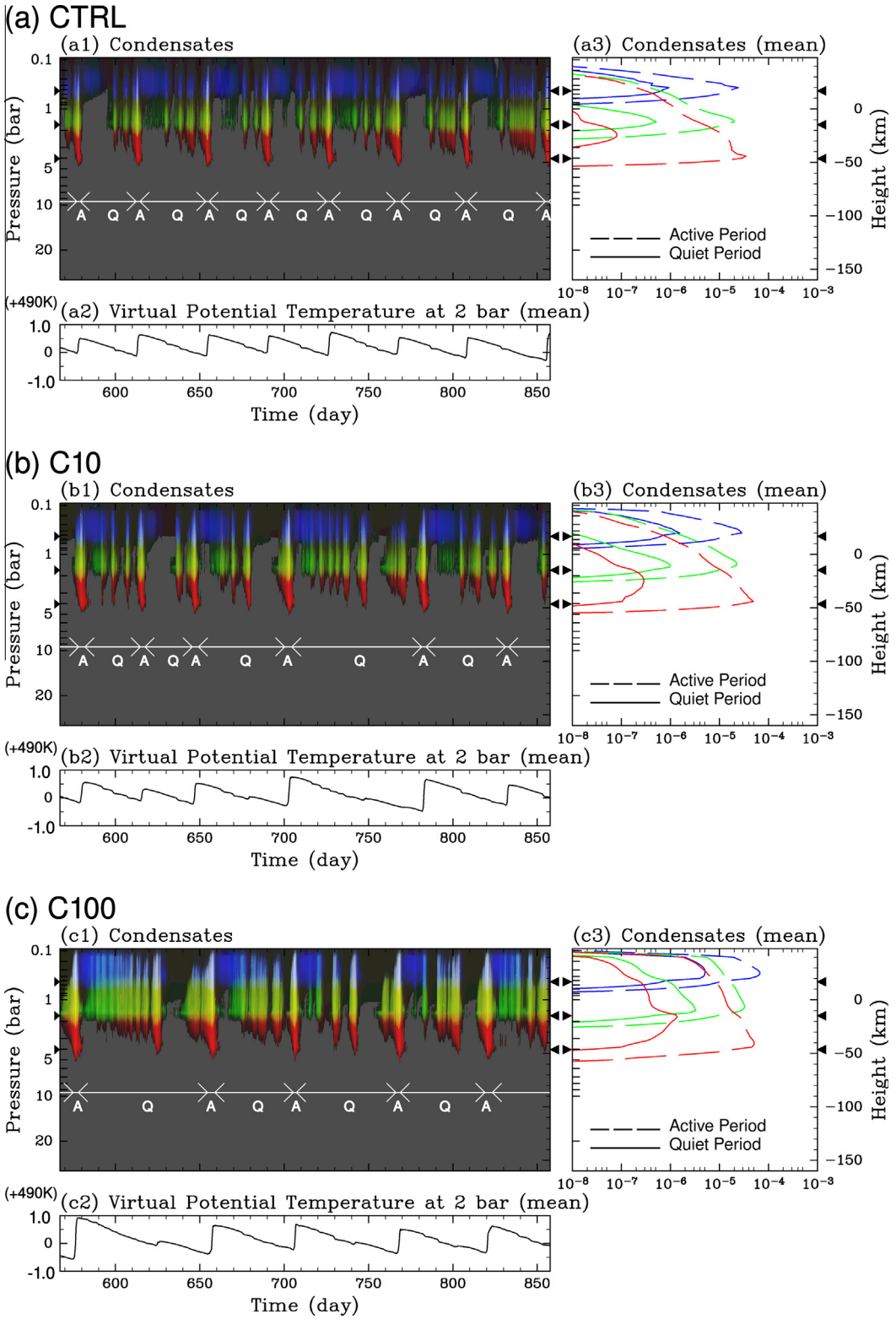

Fig. 6. (a) Temporal variations of mean mixing ratios of condensates and virtual potential temperature for CTRL. (a1) Temporal variations of horizontal mean mixing ratios of condensates plotted in the same manner as Fig. 2(a). (a2) Temporal variations of horizontal mean virtual potential temperature at $p = 2$ bar. (a3) The vertical profile of horizontal mean mixing ratios of condensates averaged only over the quiet periods and those only over the active periods. The solid and broken lines indicate profiles of quiet and active periods, respectively. (b) Same as (a) but for C10. (C) Same as (a) but for C100. Black triangles on the left and the right edges of each panel indicate the NH_3, NH_4SH, and H_2O LCLs from top to bottom for each simulation. (For interpretation of the references to color in this figure legend, the reader is referred to the web version of this article.)

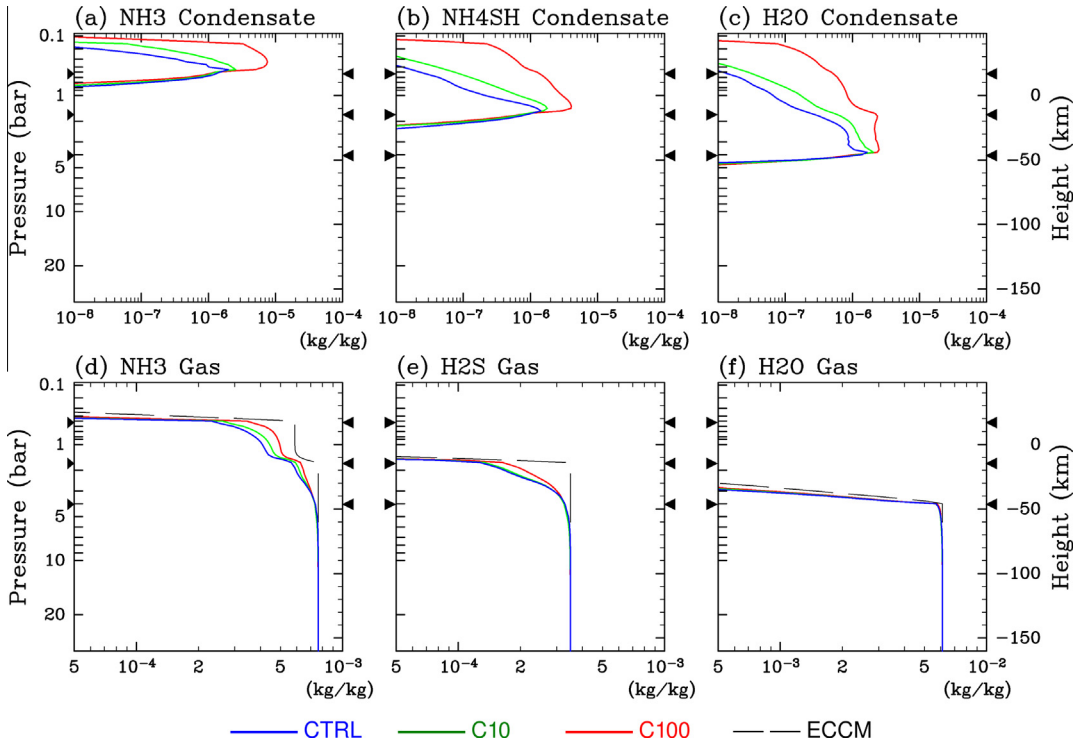

Fig. 7. Comparison of vertical profiles of horizontal mean mixing ratios of (a) NH_3, (b) NH_4SH, and (c) H_2O condensates and (d) NH_3, (e) H_2S, and (f) H_2O gases averaged over the last 4 active-quiet cycles. Blue, green, and red lines represent profiles for CTRL, C10, and C100, respectively. Thin broken lines in (d–f) represent the profiles obtained by the ECCM. Black triangles on the left and the right edges of each panel indicate the NH_3, NH_4SH, and H_2O LCLs from top to bottom. (For interpretation of the references to color in this figure legend, the reader is referred to the web version of this article.)

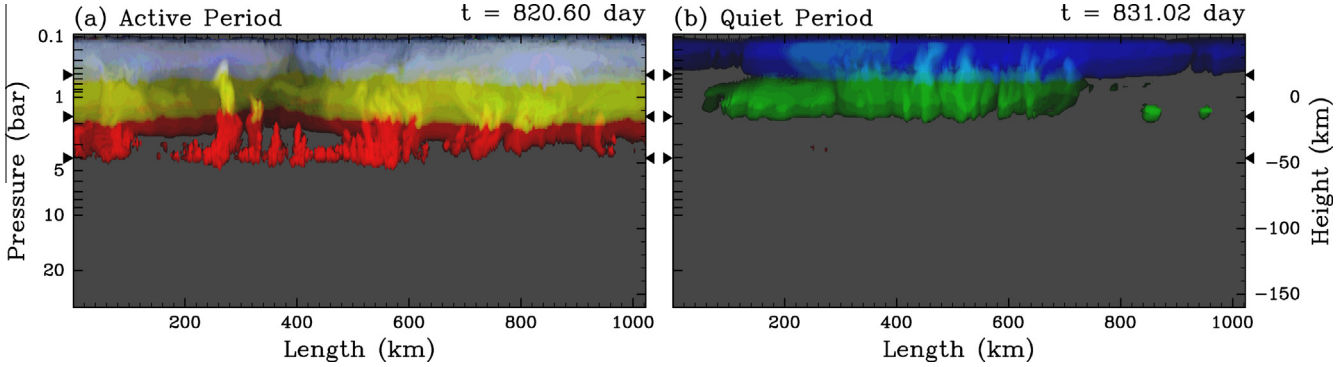

Fig. 8. Snapshots of mixing ratios of condensates obtained in C100 during (a) an active period at $t = 820.60$ day and (b) a quiet period at $t = 831.02$ day. Multiple composition condensates are represented in the same manner as in Fig. 3. Black triangles on the left and the right edges of each panel indicate the NH_3, NH_4SH, and H_2O LCLs from top to bottom.

other two cases. The values of mixing ratios in C100 are at least ten times larger than those obtained in CTRL near the tropopause. Fig. 8 shows representative snapshots of condensates in the active and quiet periods in C100. Fig. 8 indicates that the region above the NH_3 LCL is covered with condensates during the active and quiet periods.

From a comparison between τ_{auto} and the time scale of vertical advection, τ_{adv}, we can understand the reason why the amounts of condensates in C100 are much larger than those in the other two cases. According to our numerical results, a typical time scale of advection from the H_2O LCL to the tropopause, whose length scale $\Delta z \approx 8.0 \times 10^4$ m, during the active periods is $\tau^a_{adv} = \Delta z/w \approx 8.0 \times 10^4/50 = 1600$ s using the maximum vertical velocity in typical cumulonimbus clouds like that shown in Fig. 3(d3). Since the magnitude of the vertical velocity does not change greatly with τ_{auto}, we can adopt the same value of τ^a_{adv} for all cases. A typical time scale of advection from the NH_4SH LCL to the NH_3 LCL, whose length scale $\Delta z \approx 4.0 \times 10^4$ m, during the quiet periods is $\tau^q_{adv} = \Delta z/w \approx 4.0 \times 10^4/10 = 4000$ s by using the maximum vertical velocity in typical clouds like those shown in Fig. 3(b3) and (c3). We can adopt the same value of τ^q_{adv} for all cases, since the magnitude of vertical velocity also does not change greatly for the quiet periods. Now it is obvious that the values of τ^a_{adv} and τ^q_{adv} are larger than the values of τ_{auto} used in CTRL and C10, but are shorter than the value of τ_{auto} used in C100. This means, only in C100, that condensates can be advected up to the NH_3 LCL before being converted from non-precipitating to precipitating condensates, so the region above the NH_3 LCL, including downdrafts region, is covered with condensates. In CTRL and C10, even though $\tau_{auto} < \tau^a_{adv}$, the upward region can be covered with

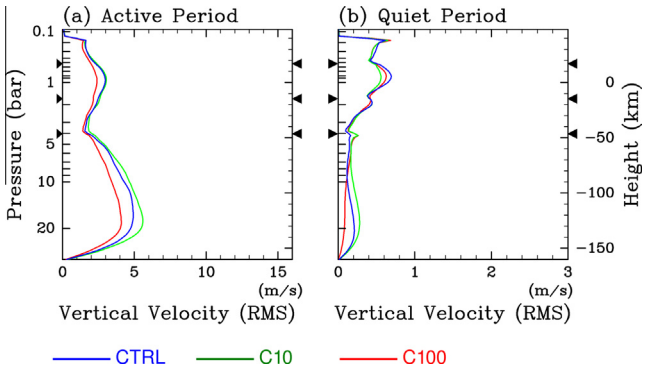

Fig. 9. Comparison of horizontal mean vertical profiles of root mean square (RMS) of vertical velocity, $\sqrt{\bar{w}^2}$, averaged (a) only over the active periods and (b) only over the quiet periods. Blue, green, red lines represent profiles of CTRL, C10, and C100, respectively. Black triangles on the left and the right edges of each panel indicate the NH_3, NH_4SH, and H_2O LCLs from top to bottom. (For interpretation of the references to color in this figure legend, the reader is referred to the web version of this article.)

condensates. This is because the terminal velocities of all precipitating condensates, which is at most 20 m/s, are smaller than the velocity of upward flow, which is typically 50 m/s.

Fig. 7(d–f) compares the horizontal mean mixing ratios of condensable gases averaged over the last 4 active-quiet cycles. The significant characteristic of the condensable gas profiles obtained by our numerical model, i.e., the mean mixing ratios of NH_3 and H_2S gases begin to decrease with height not at their respective LCLs but at the H_2O LCL, does not vary with τ_{auto}. But, the mixing ratios of NH_3 and NH_4SH gases in the moist convection layer increase with τ_{auto}. This tendency is quite obvious during the quiet periods in C100, where these gases are equilibrated with NH_3 and NH_4SH condensates that exist almost always in the moist convection layer (Fig. 6(c)).

The structure of the convective motion is, as is already mentioned above in the evaluation of time scales, qualitatively unchanged by the variation of τ_{auto}. Fig. 9(a) and (b) compare the vertical profiles of the root mean square of vertical velocity, $\sqrt{\bar{w}^2}$, averaged only over the active periods and those only over the quiet periods, respectively. The vertical profiles of $\sqrt{\bar{w}^2}$ in C10 and C100 are similar to that in CTRL for both of the periods.

5. Dependence on the deep abundances of condensable gases

In this section, the dependence of the structure and dynamics of the moist convection layer on the abundances of condensable gases at the lower boundary is examined. As is mentioned in Section 2.3, the body cooling rate used in this parameter experiment is set to be 10 times larger than that of CTRL in order to save the CPU time required to achieve statistically steady states of the model atmosphere. If we use the same cooling rate as that of CTRL for 10 times solar abundance calculation, about 10,000 h of CPU time would be required, which is beyond the computer resources available to us. This is because, as described later in this section, the period of intermittent cloud activity increases with the increasing deep abundances of condensable gases. The cloud convection obtained in R10 shares several principal features with those in CTRL except for a shorter period of intermittent cloud activity, as will be shown below. The detailed results of the parameter experiment in which the body cooling rate is varied but with the same condensable gas abundances as CTRL are described in Appendix A.

The abundances of condensable gases at the lower boundary used in this parameter experiment are summarized in Table 1. The deep abundances for R10 is the same as that for CTRL, i.e., given as the solar abundances. R10S10, R10S3, R10S01 are calculations with abundances of 10 times, 3 times, and 0.1 times solar, respectively. The heights of the LCLs depend on the deep abundances of condensable gases. For the solar composition case, as already mentioned, the LCLs of H_2O, NH_4SH, and NH_3 are about 4.0 bar, 1.7 bar, and 0.5 bar, respectively. For the 0.1 times solar case, they move toward the higher altitudes of about 2.8 bar, 1.2 bar, and 0.4 bar, respectively. For the 3 times solar case, they move toward the lower altitudes of about 4.9 bar, 1.9 bar, and 0.6 bar; and for the 10 times solar case, they go down to about 6.0 bar, 2.4 bar, and 0.7 bar, respectively.

The left panels of Fig. 10 show the temporal variations of the horizontal mean mixing ratios of condensates and virtual potential temperature at $p = 2$ bar for R10S01, R10, R10S3, R10S10, respectively. In most cases, intermittent cloud activity similar to that in CTRL is found. In R10, R10S3 and R10S10, distinct quasi-periodic cycles of cloud activity and sawtooth-like temperature variations are obtained (left panels of Fig. 10(b–d)). The exception is R10S01, where obvious quasi-periodic temporal cycle of cloud activity can not be found (left panels of Fig. 10(a)).

It should be noted that the mean period of the intermittent cycle of cloud activity is roughly proportional to the deep abundances of condensable gases. The mean periods of intermittency averaged over the last 4 active-quiet cycles are about 9, 19, and 139 days for R10, R10S3, and R10S10, respectively; their ratio is 1, 2.1, and 16, and is fairly close to the ratio for the deep abundances of 1, 3, and 10. The amplitudes of the mean virtual potential temperature variation at $p = 2$ bar during the active-quiet cycles also depend on the deep abundances of condensable gases. The amplitudes are about 0.9, 2.6, and 11 K for R10, R10S3, and R10S10, respectively; the ratio is 1, 2.9, and 12, and is also fairly close to the ratio for the deep abundances. The relationship of the period of the intermittency and the amplitude of temperature variation to the deep abundances of condensable gases will be discussed in Section 6.3.

The right panels of Fig. 10 compare the horizontal mean mixing ratios of condensates averaged only over the active periods and those only over the quiet periods. During the active periods, the peak values of the mean mixing ratios of all of the condensates have a dependence on the deep abundances of condensable gases. For example, the maximum values of mixing ratios of H_2O condensate are about 6×10^{-5}, 1.3×10^{-4}, and 5×10^{-4} kg/kg for R10, R10S3 and R10S10, respectively; the ratio is 1, 2.2, and 8.3, which again coincides with the ratio for the deep abundances of condensable gases. During the quiet period, the mean mixing ratio of H_2O condensate decreases as the deep abundances of condensable gases increase. On the other hand, the mean mixing ratios of NH_3 and NH_4SH condensates do not change much. The difference may be explained by differences in the temporal variation of condensates (see Fig. 10(b1), (c1), and (d1)); H_2O cloud activity during the quiet period is less frequent and the duration of the quiet period becomes longer as the deep abundances of condensable gases increase. The activity of NH_3 and NH_4SH clouds tends to persist even in the quiet periods, so that the change of the duration of the quiet periods matters only modestly.

Fig. 11(a–c) compares the vertical profiles of the horizontal mean mixing ratios of condensates averaged over the last 4 active-quiet cycles. The maximum value of the mean mixing ratio of each condensate is obviously insensitive to the deep abundances of condensable gases. This insensitivity can be understood from the following equation mentioned in Section 3.2, $\bar{q}_c' = \bar{q}_c'^a \Delta t^a / \Delta t$, where $\bar{q}_c'$ and $\bar{q}_c'^a$ are the mean mixing ratio of a condensate averaged over the entire active-quiet cycles and active periods, respectively, Δt is the period of the intermittency, and Δt^a is the duration of active periods. In our results, the values of Δt and $\bar{q}_c'^a$ are roughly proportional to the deep abundances of condensable gases, as is discussed above. The remaining difference can be explained by the

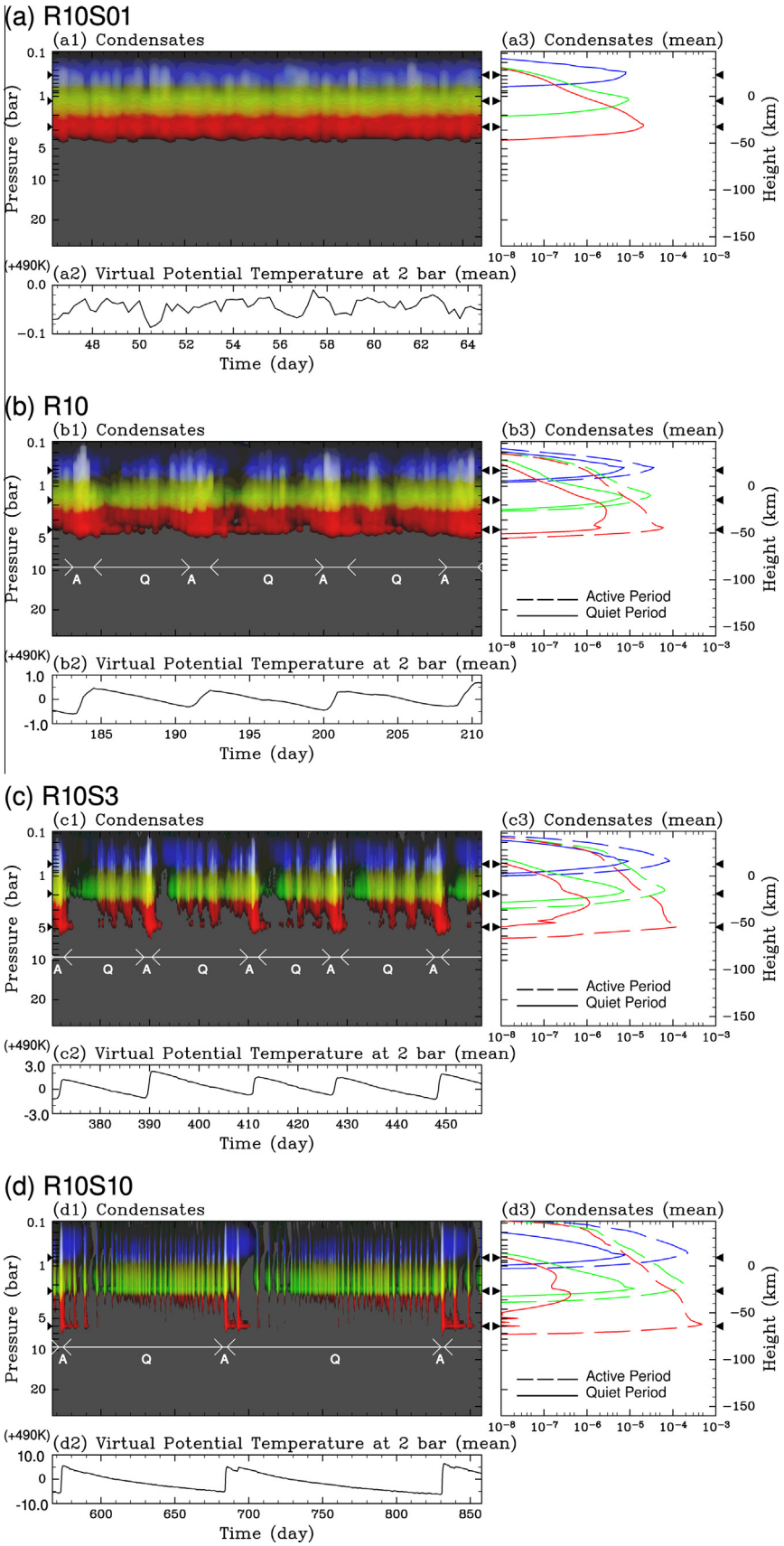

Fig. 10. Same as Fig. 6, but for (a) R10S01, (b) R10, (c) R10S3, and (d) R10S10.

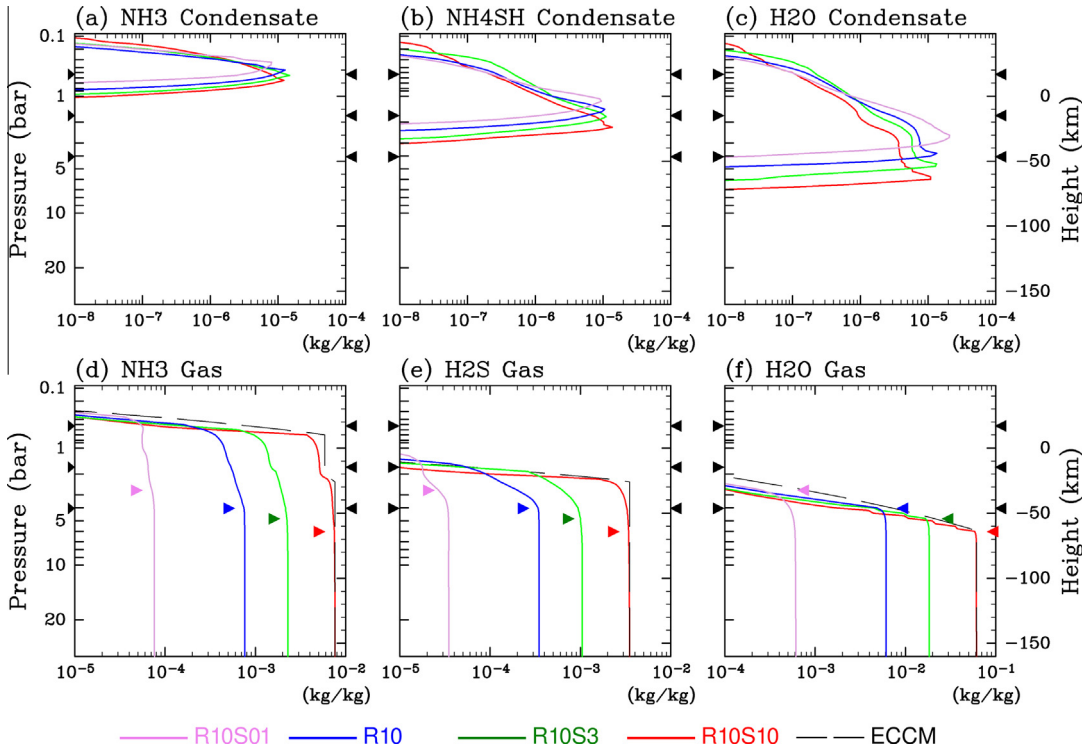

Fig. 11. Same as Fig. 7, but for R10S01, R10, R10S3, and R10S10, represented by violet, blue, green, and red lines, respectively. Thin broken lines in (d–f) represent the profiles obtained by the ECCM using the settings of R10S10. The violet, blue, green, and red triangles in (d–f) indicate the H_2O LCL for R10S01, R10, R10S3, and R10S10, respectively. (For interpretation of the references to color in this figure legend, the reader is referred to the web version of this article.)

dependence of the duration of active period on the deep abundances; the value of Δt^a is 1–2 days for CTRL and 4–5 days for R10S10 (not clearly shown here).

Fig. 11(d–f) compares the horizontal mean mixing ratios of condensable gases averaged over the last 4 active-quiet cycles. In most cases, the vertical profiles of the mean mixing ratios are similar to those in CTRL; the mixing ratio of each condensable gas begins to decrease with height from the H_2O LCL. The exception is R10S01. In R10S01, the altitude at which the mean mixing ratio of each condensable gas begins to decrease is approximately 4 bar, which is well below the H_2O LCL. This modest difference of the vertical profiles of condensable gases results from the change in vertical motion. Fig. 12 compares representative snapshots of R10 and R10S01. In R10, the vertical motion in the moist convection layer is characterized by the contrast between the narrow, strong, cloudy updrafts and the broad, weak, dry downdrafts, which resemble those in CTRL. On the other hand, in R10S01, the contrast is less definite. The widths and the intensities of the upward and downward flows are similar to each other and the convective motion resembles that of dry convection. The distributions of condensable gases of R10S01 are inhomogeneous just under the H_2O LCL. These features of the vertical motion and distribution of condensable gases observed in R10S01 imply that only the H_2O LCL acts as a weak dynamical and compositional boundary.

The convective motion characteristics in R10, R10S3 and R10S10 are fairly similar to those in CTRL. Fig. 13(a) and (b) compare the mean vertical profiles of the root mean square of vertical velocity, $\sqrt{\bar{w}^2}$, averaged only over the active periods and those only over the quiet periods, respectively. During the active periods, the vertical profiles of $\sqrt{\bar{w}^2}$ have a local minimum at the H_2O LCL in all three cases. The value of $\sqrt{\bar{w}^2}$ in the moist convection layer increases as the deep abundances of the condensable gases increase. During the quiet periods, on the other hand, the vertical profiles of $\sqrt{\bar{w}^2}$ have local minimums or inflection points at the NH_3 and NH_4SH LCLs in all of the three cases. As the deep abundances of condensable gases increase, the value of $\sqrt{\bar{w}^2}$ in the moist convection layer generally decreases, presumably because the stable layers at the LCLs strengthen. Note that the apparent sensitivity of $\sqrt{\bar{w}^2}$ in the dry convection layer results from the "contamination" of the strong circulation that occurs during the active periods, and this sensitivity should disappear if a more realistic and weaker body cooling is applied.

6. Dynamics of the quasi-periodic cloud activity

As has been examined in earlier sections, the principal feature of cloud convection in this paper is the intermittent emergence of vigorous cumulonimbus clouds. In this section, an explanation of the mechanism of the intermittency is given by considering the following three points of moist convection: (i) the trigger that causes the development of cumulonimbus clouds at the beginning of active periods; (ii) the mechanism that terminates active periods; and (iii) the factors that govern the period of the intermittent cloud activity.

6.1. Detailed temporal development at the beginning and the end of active periods

A notable characteristic of the moist convection layer observed near the end of a quiet period is rapid descent of the H_2O cloud base, which can be identified by close examination of Fig. 2(a). Fig. 14(a) shows typical snapshots of the distributions of condensates, virtual potential temperature, and wind vectors around the H_2O LCL superposed on relative humidity near the end of a quiet period. As indicated by the nearly homogeneous virtual potential temperature (Fig. 14(a3)), the atmosphere is neutral to dry convection from the NH_4SH LCL down to the altitudes just above the H_2O LCL. The downward plumes produced by the evaporation of H_2O condensate can easily go down to the altitudes near the H_2O LCL

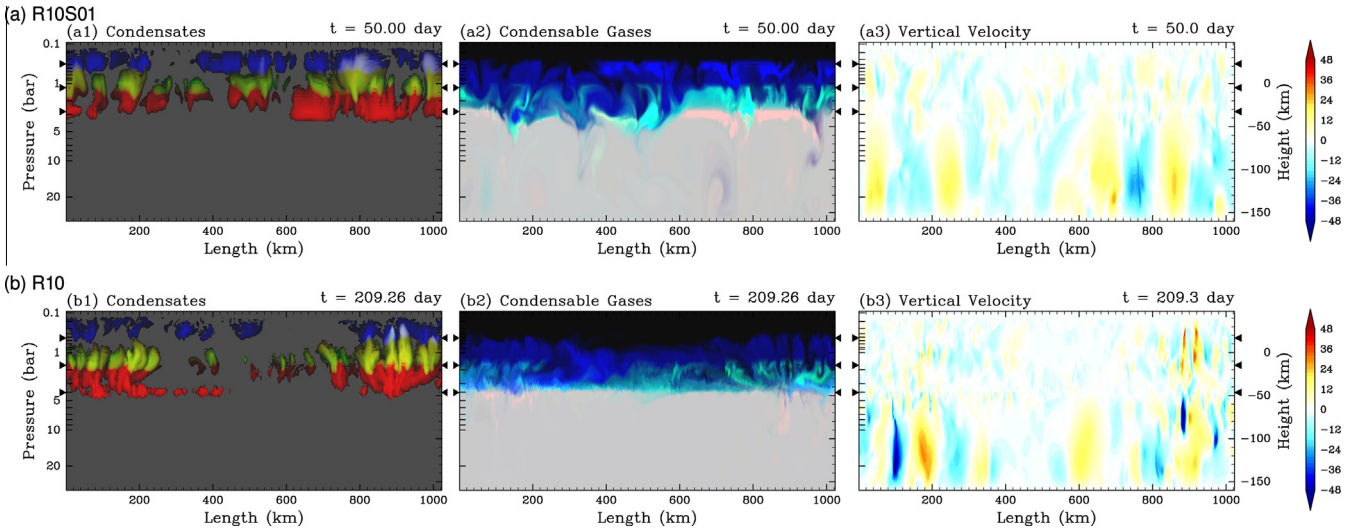

Fig. 12. (a) Snapshots in R10S01. (a1) Mixing ratios of condensates plotted in the same manner as in Fig. 3. (a2) Mixing ratios of condensable gases plotted in the same manner as in Fig. 3. (a3) Vertical velocity. (b) Same as (a) but for an active period in R10. Black triangles on the left and the right edges of each panel indicate the NH_3, NH_4SH, and H_2O LCLs for each simulation.

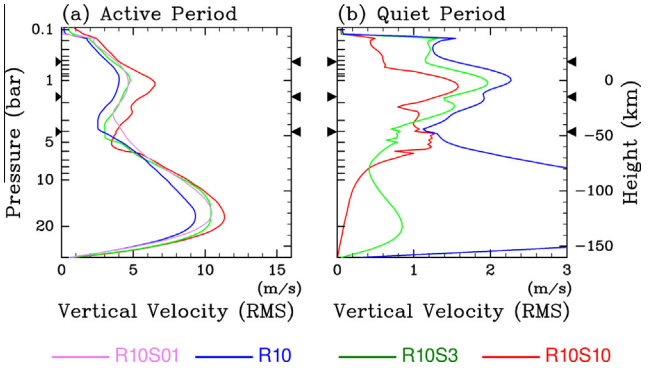

Fig. 13. Same as Fig. 9 but for R10S01, R10, R10S3, and R10S10, represented by violet, blue, green, and red lines, respectively. Note that R10S01 is regarded to consist only of active period. (For interpretation of the references to color in this figure legend, the reader is referred to the web version of this article.)

and cool the region below the NH_4SH LCL. Moist air in the vicinity of these downward plumes rises with the returning upward motions due to mass continuity, and forms H_2O clouds, resulting in the successive formation of H_2O clouds indicated by the tilted H_2O cloud bases in Fig. 14(a1). At this stage, vertical motion near the H_2O LCL is weak and the region near the LCL is unsaturated (Fig. 14(a2)).

Characteristic snapshots at the transition from the quiet period to the active period are shown in Fig. 14(b). A noteworthy feature is that precipitating H_2O condensate begins to fall below the H_2O LCL ($x \sim 300$ km of Fig. 14(b1)). At this stage, the vertical motion near the H_2O LCL is still weak and the region near the LCL is still unsaturated (Fig. 14(b2)).

An outbreak of vigorous cumulonimbus clouds at the beginning of the active period is shown in Fig. 14(c). H_2O condensate falls down below the H_2O LCL. There are upward and downward flows penetrating through the H_2O LCL, which can be observed under the base of the vigorous cumulonimbus clouds (arrows in Fig. 14(c2)). Relative humidity near the H_2O LCL is highly inhomogeneous (tone in Fig. 14(c2)). Virtual potential temperature in a cumulonimbus cloud ($x \sim 250$ km of Fig. 14(c3)) is higher than that of the surrounding region, implying that the cumulonimbus cloud is significantly buoyant. Fig. 14(d) shows snapshots at the peak of the active period. Two or three intense cumulonimbus towers develop simultaneously. The overall features of the structure and dynamics of the moist convection layer do not significantly change from those at the beginning of the active period shown in Fig. 14(c), except the overall rise of virtual potential temperature in the upper half of the moist convection layer (Fig. 14(d3)) due to the release of the latent heat of condensation in the vigorous cumulonimbus clouds.

Approaching the end of the active period (Fig. 14(e)), overall virtual potential temperature increases even in the lower half of the moist convection layer (Fig. 14(e3)). Virtual potential temperature observed in the cumulonimbus clouds base ($x \sim 600$ km of Fig. 14(e3)) is obviously lower than that of the surrounding regions, although that is still higher in the upper half of the moist convection layer. This negative anomaly of the virtual potential temperature mainly results from the large amount of condensable gases and condensates observed in the cumulonimbus cloud. Finally at the end of the active period (Fig. 14(f)), a further rise in the virtual potential temperature of the moist convection layer almost completely eliminates the buoyancy in clouds (Fig. 14(f3)); a developing cloud at around $x = 950$ km of Fig. 14 (f1) is no longer able to reach to the tropopause.

6.2. The conditions at the beginning and the end of active periods

The rapid development and large buoyancy of the cumulonimbus clouds at the beginning of the active period described above suggests that an ample amount of instability is accumulated before the beginning of the active period. Tapped by a certain triggering mechanism, the instability is abruptly released and vigorous cumulonimbus clouds develop. On the other hand, the end of active periods seems to result from the decrease of the instability, and the instability is completely exhausted at the transition to the quiet period which follows.

In order to analyze the conditions at the beginning and the end of active periods further, a quantitative definition of the instability is necessary. We can define an integral measure of convective instability considering that development of cumulonimbus clouds requires the existence of a negative pressure anomaly at the foot of the updraft, which accelerates horizontally converging wind near the cloud base. Indeed, Fig. 15(a) indicates that there is a negative pressure anomaly near the cumulonimbus clouds base at around $x = 600$ km at the time shown in Fig. 14(e1). Fig. 15(b) indicates

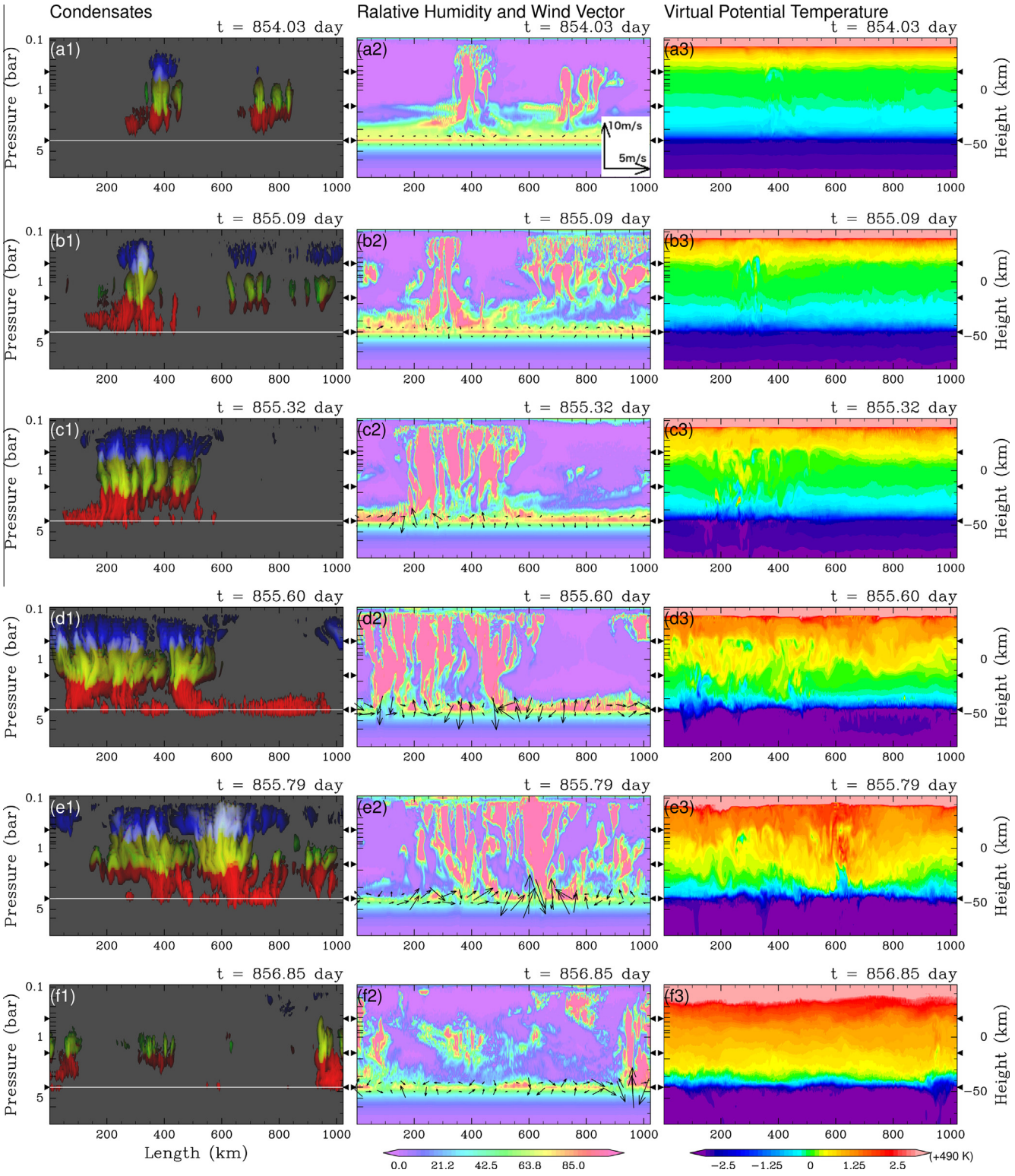

Fig. 14. Snapshots of (∗1) mixing ratios of condensates, (∗2) wind vector near the H_2O LCL superposed on relative humidity, and (∗3) virtual potential temperature obtained in CTRL. Each line of panels cover from (a) just before the start to (f) the end of an active period. Multiple compositions of condensates are represented in the same manner as in Fig. 3. Black triangles on the left and the right edges of each panel indicate the NH_3, NH_4SH, and H_2O LCLs, and white thin lines in (∗1) also indicate the H_2O LCL.

that the cloud at the end of the active period, located at around $x = 950$ km (see Fig. 14(f1)), is also associated with a negative pressure anomaly, but the anomaly is weak and the center of the anomaly is deviated from the cloud.

We vertically integrate Eq. (5) neglecting time-dependent terms and subgrid turbulence term, the difference between the values of the Exner function at the tropopause and the H_2O LCL can be expressed as

$$\int_{\pi_{H_2O}}^{\pi_{top}} d\pi' = \int_{z_{H_2O}}^{z_{top}} \frac{1}{c_{p_d}\theta_{v0}}\left(\frac{\theta'_v}{\theta_{v0}}\right) g\, dz, \tag{10}$$

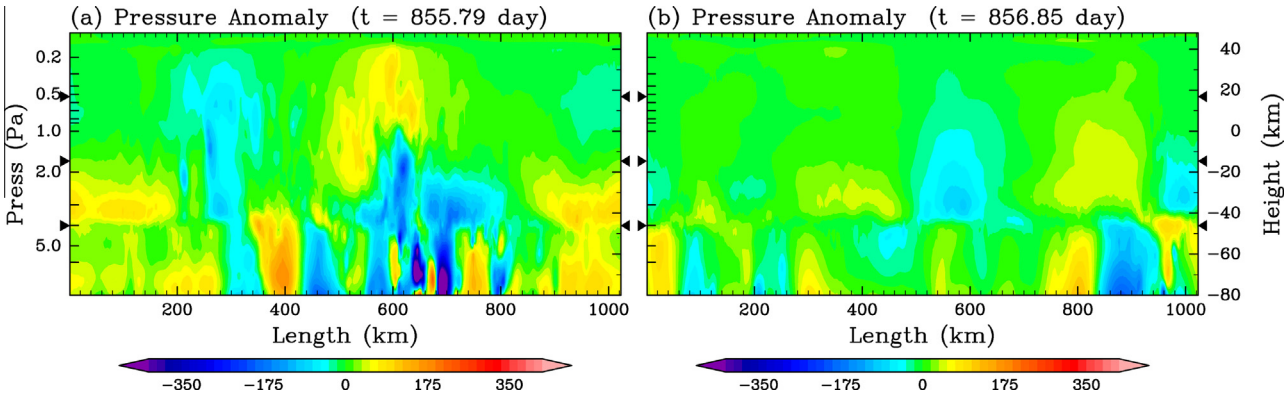

Fig. 15. The distributions of pressure anomaly, defined as the deviation from the horizontal average, at the time shown in Fig. 14(e) and (f).

where π_{top} and π_{H_2O} are the values of the Exner function at the tropopause and the H_2O LCL, respectively, and z_{H_2O} and z_{top} are the altitudes at the tropopause and the H_2O LCL, respectively. By applying Eq. (10) to an active updraft and surrounding environment and taking the difference, assuming the pressure difference at the tropopause to be zero, we obtain a reasonable maximum intensity of the pressure anomaly at the H_2O LCL as

$$(\pi^{\prime *}_{H_2O} - \pi^{\prime \dagger}_{H_2O}) = \int_{z_{H_2O}}^{z_{top}} \frac{g}{c_{p_d}\theta_{v0}} \left(\frac{\theta^{\prime *}_v - \theta^{\prime \dagger}_v}{\theta_{v0}} \right) dz, \tag{11}$$

where the variables denoted by an asterisk and a dagger represent a rising air parcel in an active updraft and surrounding air, respectively. By rewriting Eq. (11) in terms of pressure and virtual temperature, we define the integral measure of convective instability, A, as

$$A \equiv (p^{\prime *}_{H_2O} - p^{\prime \dagger}_{H_2O}) = \int_{z_{H_2O}}^{z_{top}} \rho_0 g \left(\frac{T^{\prime *}_v - T^{\prime \dagger}_v}{T_{v0}} \right) dz. \tag{12}$$

Fig. 16 shows the temporal variations of A in CTRL, C10, C100, R10, R10S3, and R10S10. In order to estimate the value of T^*_v and $T^\dagger_v$ in Eq. (12), we have to assume the vertical profiles of temperature, condensable gases, and condensates. As for the rising air parcel, the profiles of temperature and condensable gases are assumed to follow the moist adiabat of the rising air parcel from just below the H_2O LCL, and the temporal variation of the vertical profiles of condensates are given by those of peak values observed in our simulations. As for the surrounding air, the temporal variations of all of the profiles are given by horizontal mean profiles observed in our simulations; the resulting temporal variation of $T^\dagger_v$ shows sawtooth-like variation similar to that observed in horizontal-mean virtual potential temperature (Fig. 6(a2), (b2), and (c2); Fig. 10(b2), (c2), and (d2)). In each case, A shows a sawtooth-like temporal variation, which is similar to the variation of horizontal-mean virtual potential temperature in the moist convection layer upside down. This suggests that a considerable portion of the variation of A results from the variation of virtual temperature of the surrounding air.

An important feature commonly found in all cases is that the values of A become almost zero at the end of the active periods (Fig. 16). This proves that exhaustion of the convective instability is indeed the criterion for the end of the active periods. Re-examination of the distribution of virtual potential temperature just before the end of the active period (Fig. 14(e3)) indicates that the condition $A = 0$ is not realized as $\theta^{\prime *}_v - \theta^{\prime \dagger}_v = 0$ at every altitude in the moist convection layer, but is realized as a cancellation of the positive buoyancy, $(\theta^{\prime *}_v - \theta^{\prime \dagger}_v)g/\theta_{v0} > 0$, in the upper levels and the negative buoyancy, $(\theta^{\prime *}_v - \theta^{\prime \dagger}_v)g/\theta_{v0} < 0$, in the lower levels. The negative buoyancy in the lower levels results from the large mixing ratios of condensates and condensable gases, whose molecular weight is larger than that of the dry air of Jupiter's atmosphere.

It should be noted that, in all cases, a considerable amount of positive A is accumulated before the beginning of the active periods (Fig. 16). It is also notable that the value of A returns to positive more or less quickly after the end of the active periods, at which the value of A is zero. These features clearly indicate that the accumulation of instability is not a sufficient but a necessary condition for the onset of the active period. As was discussed in Section 6.1, the trigger is H_2O condensate that falls down through the stable layer at the H_2O LCL by gravitational settling (see Fig. 14). H_2O condensate evaporates and cools the surrounding air below the H_2O LCL by the negative latent heat and drives downward plumes. These downward plumes induce compensating updrafts that carry air parcels containing large amounts of condensable gases from below the H_2O LCL. The ascending air parcels form the outbreak of the vigorous cumulonimbus clouds. The gravitational settling of H_2O condensate is indispensable to the trigger because, without this process, evaporation cooling below the H_2O LCL, which drives the ascent of moist parcels crossing the stable layer at the H_2O LCL, would be impossible.

Of course, in order for an appreciable amount of precipitating H_2O condensate to travel down to below the H_2O LCL before being evaporated out, clouds have to develop from a low enough level. This is realized by successive formation of H_2O clouds with the help of downward plumes as shown in Fig. 14(a1) and (b1). The descent of plumes requires a nearly neutral environment. Thus, the final "sufficient" condition for the trigger to work is the decrease of the stability just above the H_2O LCL as is indeed realized in Fig. 14(a3) and (b3).

6.3. Period of intermittency

The period of intermittency Δt, which is approximately the duration of the quiet period, can be roughly estimated using both the magnitude of the temperature change during the quiet period, ΔT, and the body cooling rate, Q_{rad}, which is the primary thermal forcing during the quiet periods (Fig. 4). The following expression is then satisfied:

$$\int_{p_{H_2O}}^{p_{top}} \frac{c_{p_d}}{g} \Delta T \, dp = \int_{p_{rad}}^{p_{top}} \frac{c_{p_d}}{g} Q_{rad} \Delta t \, dp, \tag{13}$$

where p_{rad} is the pressure level of the bottom of the radiative region. Because c_{p_d} and Q_{rad} are constant in our model and the values of p_{H_2O} and p_{rad} are much larger than that of p_{top} (e.g., $p_{H_2O} = 4$ bar for CTRL, $p_{rad} = 2$ bar, and $p_{top} = 0.1$ bar), Eq. (13) can be approximated as,

$$\Delta t \approx \frac{\overline{\Delta T}}{Q_{rad}} \frac{p_{H_2O}}{p_{rad}}, \tag{14}$$

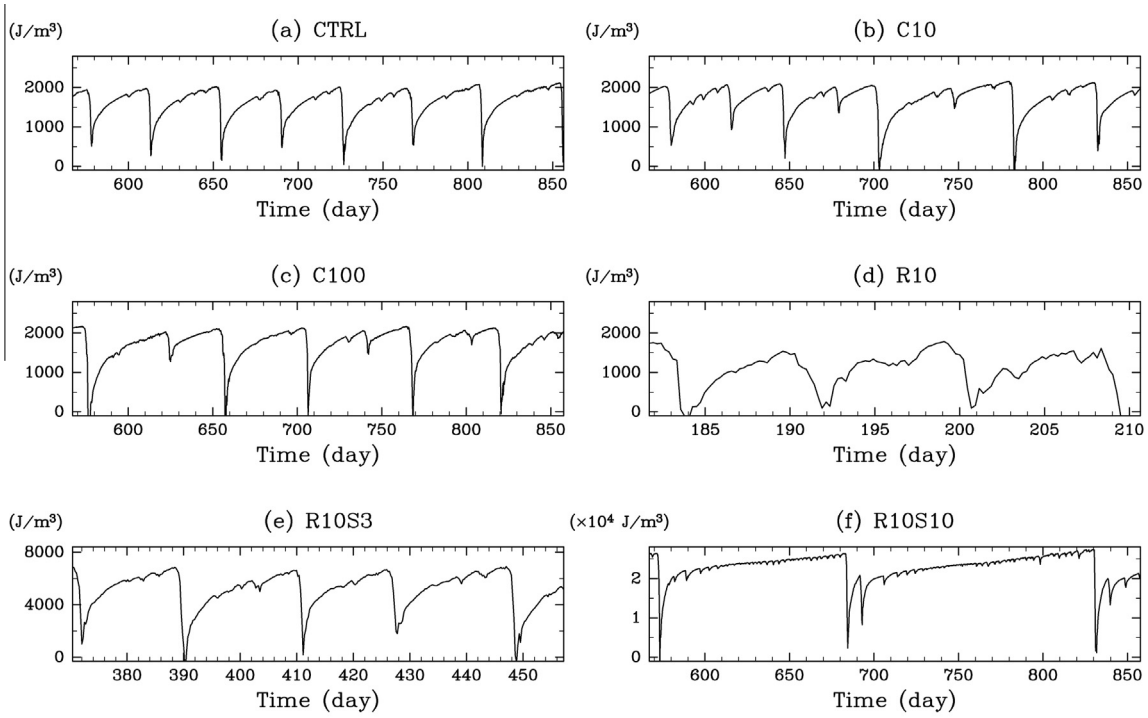

Fig. 16. Temporal variation of the integral measure of convective instability given by Eq. (12) in (a) CTRL, (b) C10, (c) C100, (d) R10, (e) R10S3, and (f) R10S10.

Table 2
Summary of intermittent cloud activity.

Run	Mean period (results)	Values of each terms included in Eq. (14)		
		p_{H_2O}	$\overline{\Delta T}$	Δt
CTRL	41	4.0	0.29	58
C10	54	4.0	0.33	65
C100	61	4.0	0.42	84
R3	17	4.0	0.3	20
R10	9	4.0	0.44	8.9
R10S3	19	4.9	0.94	23
R10S10	139	6.0	3.9	116

where

$$\overline{\Delta T} = \frac{1}{p_{H_2O}} \int_{p_{H_2O}}^{p_{top}} \Delta T \, dp.$$

Eq. (14) gives an estimate of the period of intermittency. The periods of intermittency realized in the numerical experiments are summarized and their estimates based on Eq. (14) are provided in Table 2. The values of $\overline{\Delta T}$ are also evaluated from the results of the numerical simulations. The estimated period for each case explains the result of each numerical calculation reasonably well.

Table 2 indicates that the period of intermittency is roughly proportional to the deep abundances of condensable gases, since $\overline{\Delta T}$ is also roughly proportional to the deep abundances of condensable gases. The dependence is actually stronger than what the proportionality predicts. The remaining tendency can be explained by the dependency of p_{H_2O} on the deep abundances. The value of p_{H_2O} observed in R10S10 is 1.5 times larger than that in CTRL. Additionally, the results of a parameter experiment with different intensities of body cooling, which are presented in the Appendix A, show that the period of intermittency is roughly inversely proportional to the intensity of body cooling, although an error factor of 2 remains resulting from the moderate dependence of $\overline{\Delta T}$ on the cooling rate. As for the value of $\overline{\Delta T}$, we have not succeeded in deriving its analytic expression yet. At the moment, no further pursuit is being undertaken to relate analytically $\overline{\Delta T}$ to the deep abundances of condensable gases and the body cooling rate. If we tentatively accept the dependence of the period of intermittency on the deep abundances and the cooling rate, we can very roughly estimate the periods of intermittency as around 200 days for 3 times solar and around 1000 days for 10 times solar in the case of using the same body cooling rate for CTRL.

Finally, it is worth considering the dependence of the period of intermittency on the autoconversion time scale. The difference in $\overline{\Delta T}$ for CTRL, C10, and C100 (Table 2) results mainly from the difference of virtual potential temperatures at the beginning of the active period (see Fig. 6); virtual potential temperatures at the end of the active periods are almost the same. The sensitivity of virtual potential temperature at the beginning of the active period to the autoconversion time scale can be understood as described below. As was shown in Fig. 14, the beginning of the active period is characterized by the development of cumulonimbus clouds triggered by the precipitating H_2O condensate falling down below the H_2O LCL. In order for this to happen, an appreciable amount of precipitating H_2O condensate must be produced at heights suitable for it to fall below the H_2O LCL before evaporation. Apparently, this condition is more easily satisfied with a shorter autoconversion time scale. In other words, in the case of a longer autoconversion time scale, a lower temperature of the moist convection layer, which leads to a further decrease of the stability just above the H_2O LCL, is required to have an appreciable amount of H_2O condensate at a suitable level for precipitation down to below the H_2O LCL.

7. Concluding remarks

In this paper, we have examined the idealized structure and dynamics of Jupiter's moist convection layer by using a two-dimensional numerical model, as well as their dependences on the autoconversion time scale and the deep abundances of condensable gases. Although the model used in the present study explicitly solves dynamical processes and includes thermodynamical and microphysical processes for all three important condensates in Jupiter's atmosphere, it contains several assumptions and simplifications that are not necessarily supported by physical prin-

ciples or observations. Thus, in this section, we try to make only qualitative comparisons and discussion about some observations. Of course, future studies will be indispensable to determine whether these comparisons are really appropriate or not. Observation of the physical properties of clouds below the visible cloud deck, in particular, is critically demanded.

In all of the cases described in this paper, vigorous cumulonimbus clouds develop from the H_2O LCL to above the NH_3 LCL. The existence of vigorous cumulonimbus clouds is supported by several recent observational studies (Gierasch et al., 2000; Simon-Miller et al., 2000; Sromovsky and Fry, 2010). The possibility of the cumulonimbus clouds development has been discussed in the previous theoretical and numerical studies on convection of a single cloud (Stoker, 1986; Yair et al., 1992, 1995; Hueso and Sanchez-Lavega, 2001). We emphasize here that vigorous cumulonimbus clouds are ubiquitous entities in a statistically steady state of our simulations that is free from any arbitrary choice of the initial conditions. The present study has firmly established that vigorous cumulonimbus clouds are "ordinary" entities in Jupiter's atmosphere.

A notable feature of the cumulonimbus convection realized in this study is that they develop successively as a "mesoscale convective system" with a lifetime of 1–2 day for CTRL and 4–5 days for R10S10. This feature is also supported by several recent observational studies. Based on cloud imaging (Li et al., 2004) and observations of lightning (Dyudina et al., 2004), it is known that cumulonimbus clouds in Jupiter's atmosphere develop with a lifetime of about 3.5 days, which is significantly longer than the lifetime of individual convective cells, about 3 h, simulated in the numerical simulations in the past (e,g., Yair et al., 1995; Hueso and Sanchez-Lavega, 2001). Gierasch et al. (2000) illustrates a schematic view of cloud system of Jupiter's atmosphere based on observations by Galileo, which consists of various developing convective cells. A closer comparison with the observational studies would require numerical calculations using three-dimensional numerical models, so this is a subject for future research.

Another observational fact which the present study may explain is the global average vertical distribution of NH_3. It is known but has remained difficult to explain that the abundance of NH_3 is globally subsaturated around the NH_3 cloud top ($0.4\ \text{bar} < p < 0.6\ \text{bar}$) and is subsolar by a factor of 2 below the NH_3 cloud base ($0.6\ \text{bar} < p < 2\ \text{bar}$) (de Pater et al., 2001; Gibson et al., 2005; Showman and de Pater, 2005). Interestingly, the mean vertical profiles of NH_3 gas obtained in the present study coincide fairly well in all cases. Our calculations suggest that the observed low NH_3 abundance is the result of the compensating downward motion associated with the intense cumulonimbus clouds that carries very dry air near the tropopause down to the H_2O LCL.

On the other hand, the present results do not reproduce the observation made by the Galileo probe that all condensable gases are depleted below the H_2O LCL (Wong et al., 2004). In all cases other than R10S01, dry air parcels can rarely penetrate below the H_2O LCL, since the H_2O LCL acts as a strong dynamical and compositional boundary, so the region below this level is kept homogeneously wet. In R10S01, since the H_2O LCL acts as a weak dynamical and compositional boundary, dry air parcels can reach to below the H_2O LCL, but the region below 4 bar level is also kept homogeneously wet (Fig. 12). Explanation of the Galileo probe observation would require some large-scale processes such as large-scale vortical wave disturbances (Showman and Dowling, 2000; Friedson, 2005) or meridional circulations, which are not considered in this study.

The intermittent cloud activity obtained in our experiments may be relevant to the observed "fading/revival" cycle in some of the major belts on Jupiter (Rogers, 1995; Sanchez-Lavega et al., 2008; Fletcher et al., 2011), which are associated with significant temporal variations of cloud activity. The temperature variation in the troposphere ($p > 0.3$ bar) observed by Fletcher et al. (2011), warm in the period with cumulonimbus clouds and cool in the period without cumulonimbus clouds, seems to be consistent with the present results. The episodic emergence of giant convective storms of Saturn (Fischer et al., 2011) may also be understood as an analog of the intermittent cloud activity in the present model. However, the intermittency found in this study and the observed fading/revival cycle of Jupiter's atmosphere differ at least in the following respects. First, the typical period of convective activity in the present study, e.g., the mean period of about 41 days in CTRL, differs considerably from that of the fading/revival cycle of Jupiter's belts, 3–10 years. Using the dependences on the deep abundances of condensable gases and the body cooling rate, which are discussed in Section 6.3, the observed time scale of the fading/revival phenomena could be reproduced by assuming a value about 10–30 times solar for the deep abundance of H_2O gas; if extrapolating the rough proportionality between the periods of the intermittent cloud activity and the deep abundances of condensable gases, the estimated abundance would be about 20–30 times solar based upon the result of CTRL. In addition, if scaling the period observed in R10S10 to the realistic body cooling rate, the estimated abundance would be about 10–15 times solar. These large enhancements are within the range predicted by the "clathrate hydrate scenario" for the formation of Jupiter (Gautier et al., 2001; Hersant et al., 2004)[1], and are somewhat close to the value deduced by Ingersoll and Kanamori (1995) (see [1]) from the propagation property of atmospheric waves excited by the collisions of Comet Shoemaker-Levy 9 in 1994. The JUNO mission is expected to find clues for assessing the deep abundances. Second, the cloud activity in the intermittency in the present model and that of the observed revival/fading cycle in South Equatorial Belt evolve differently; in the former, short outbreaks occur separated by long quiet periods, but in the latter, more or less steady convective activity continues in the "normal" period, followed by an interval of quiescence ("fading") that is then abruptly shifted to a short, very intense activity ("disturbance"), which returns to the "normal" state of moderate activity. The evolution of convective activity in the North Temperate Zone (Sanchez-Lavega et al., 2008) is more similar to that in the present study. The variety above may arise from the interaction between the convection and the large-scale motions in the real Jupiter's atmosphere such as possible meridional circulation associated with belt-zone structure or the large scale eddies. Exploration of this issue is left for a future three-dimensional numerical study.

The existence of lightning flashes also may provide a hint to the abundance of H_2O in the deep atmosphere because active charge separation is possible only in strong cumulonimbus clouds with large amount of condensates, whose development requires a large mixing ratio of H_2O gas (Gibbard et al., 1994; Yair et al., 1995, 1998). Gibbard et al. (1994) argues that a density of at least $1-2\times10^{-3}\ \text{kg/m}^{-3}$ of H_2O condensate is necessary for the development of a thunderstorm. In CTRL, the maximum mixing ratio of H_2O condensate in the cumulonimbus clouds developed in the active periods is nearly equal to this threshold, but the maximum mixing ratio in the quiet period is obviously smaller. During the active period, since the maximum mixing ratio of H_2O condensate is about 4×10^{-3} kg/kg (see Section 3.1) and the air density at the H_2O LCL is about 0.4 kg/m^3, the maximum density of H_2O condensate is about 1.6×10^{-3} kg/m^3. Thus, the present result implies that one time solar value of H_2O is the threshold for lightning, being also consistent with the results of Yair et al. (1998)[1]. Of

[1] Note that the solar abundance considered in previous studies is that reported by Anders and Grevesse (1989); the abundance of oxygen reported by Grevesse et al. (2007) used in our calculations is about twice as small as that reported by Anders and Grevesse (1989).

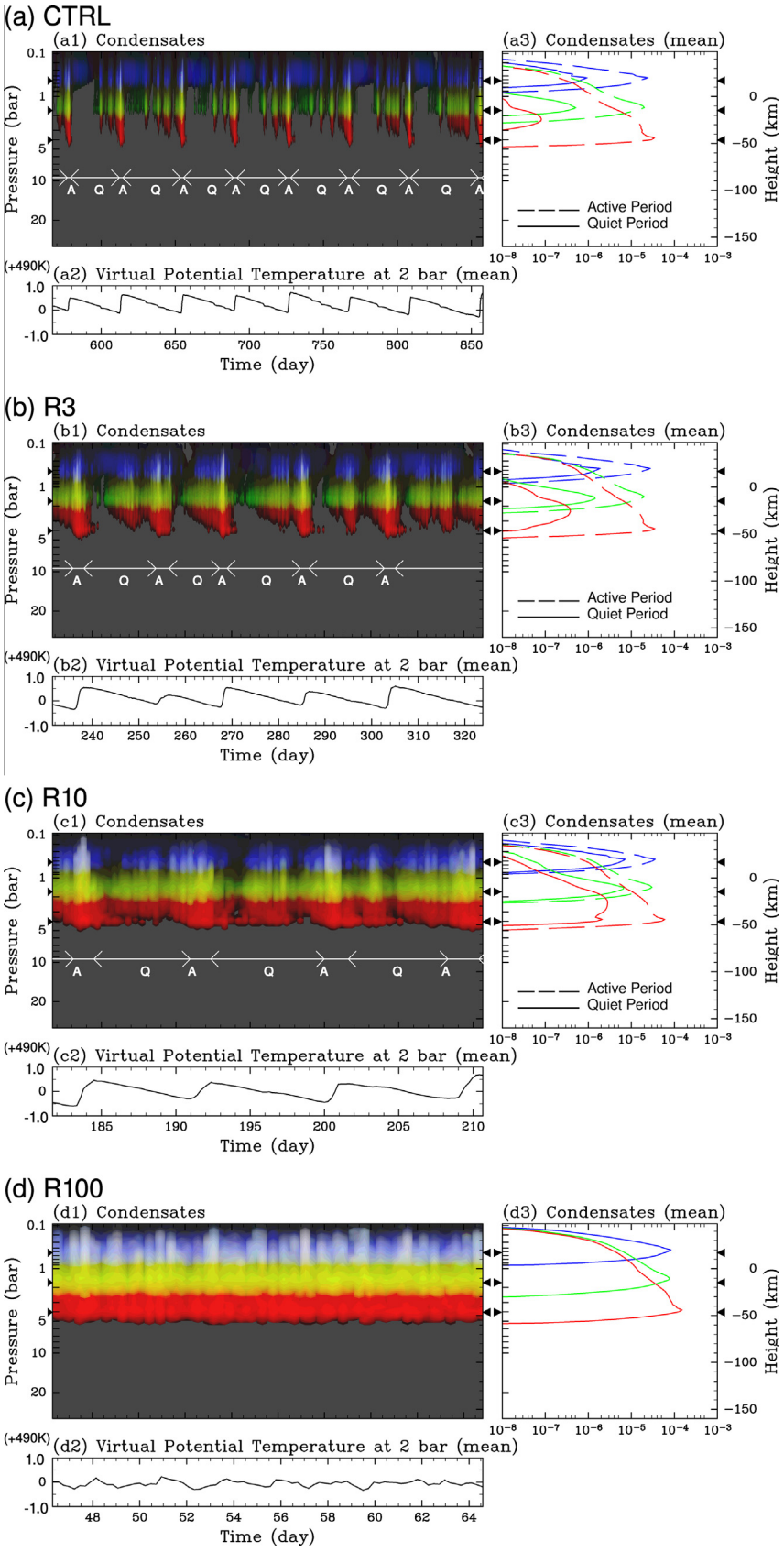

Fig. 17. Same as Fig. 6 but for (a) CTRL, (b) R3, (c) R10, and (d) R100.

course, the discussion above remains very crude, and more quantitative investigation requires implementation of charge generation models such as used in Yair et al. (1998).

One way which the present model is distinctly different from observational data is that the upper troposphere is almost always clear in most cases (e.g., Fig. 3 for CTRL) as opposed to the real

atmosphere of Jupiter, which is covered globally with a visible cloud deck. This may result partly from the value of the threshold mixing ratio for the autoconversion process being set to zero (see Section 2.3). If using a non-zero value of the threshold for NH_3 condensate, the upper troposphere would be completely cloudy. In order to explain the presence of the widespread cloud deck in the upper troposphere, an improvement of the bulk parameterization scheme to include possible categories of icy particles, i.e., cloud, ice crystals, snowflakes, graupel, and hail, for all of the three condensates, and interaction among different condensates would be necessary, but this is one of the issues for the future, when in situ observations and realistic laboratory experiments of Jupiter's clouds will be possible.

Acknowledgments

Numerical computations were carried out on Cray XT4 at Center for Computational Astrophysics, National Astronomical Observatory of Japan. The authors would like to thank Dr. Manabu Yamada for his suggestions concerning visualization and Dr. Yoshiyuki O. Takahashi, Dr. Seiya Nishizawa, Dr. Masaki Ishiwatari, and Dr. Shin-ichi Takehiro for useful comments. Products of GFD Dennou Club (http://www.gfd-dennou.org/), including Dennou Club Library (DCL), Dennou Ruby Project tools, and the gtool5 library, are used in this study. This work was supported by grants-in-aid (24740316 and 23103003) from the Ministry of Education, Culture, Sports, Science and Technology in Japan.

Appendix A. Dependence on the body cooling rate

In this appendix, the dependence of the structure and dynamics of the moist convection layer on the externally-given body cooling rate, Q_{rad}, which is a substitute for radiative cooling, is investigated. This additional investigation is necessary, as an large value of Q_{rad} is used in the parameter study examining the dependence on the deep abundances of condensable gases in Section 5. This section may also be useful for extending the applicability of this study to the atmospheres of a class of extra solar planets, "Hot Jupiter." We have performed two extra runs, R3 and R100. The values of the parameters for numerical simulations are also listed in Table 1.

The left panels of Fig. 17 show the temporal variations of the horizontal mean mixing ratios of condensates and virtual potential temperature at $p = 2$ bar for CTRL, R3, R10, and R100, where the values of Q_{rad} are 0.01, 0.03, 0.1, and 1.0 K/day, respectively. The intermittent cloud activity develops in all cases except for R100. The results in R100 (Fig. 17(d)) are consistent with those of Sugiyama et al. (2009), where the same value of cooling rate is employed and no obvious quasi-periodic temporal cycle appears. As for the temporal variations for R3 and R10, there appear intermittent vigorous cumulonimbus clouds marked as "A" in Fig. 17(b1) and (c1), and a sawtooth-like variation of potential temperature synchronizing with the intermittent cloud activity (Fig. 17(b2) and (c2)). The periods of intermittency averaged over the last 4 active-quiet cycles observed in CTRL, R3, and R10 are about 41, 17, and 9 days, respectively.

The most remarkable difference between R10 and CTRL is the vertical distribution of condensates during the quiet periods. The right panels of Fig. 17 show the vertical profiles of the condensates averaged only over the active periods and those only over the quiet periods. Although the vertical profiles for the active periods in R10 and in CTRL are similar, the peak values during the quiet periods in R10 are considerably larger than those in CTRL, and in R10, a small amount of H_2O and NH_4SH cloud particles continue to exist even above the NH_3 LCL during the quiet period. Clouds of all kinds of condensates continue to form throughout the time integration in R10 (Fig. 17(c1)), whereas there are intervals in which no H_2O or NH_4SH clouds are present in CTRL (Fig. 17(a1)).

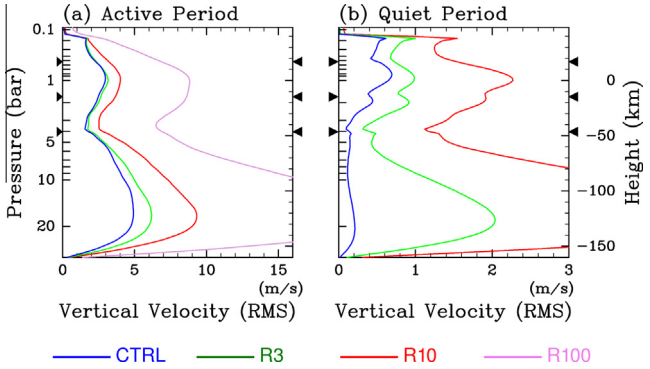

Fig. 18. Same as Fig. 9 but for CTRL, R3, R10, and R100, represented by blue, green, red and violet lines, respectively. Note that R100 is regarded to consist only of active period. (For interpretation of the references to color in this figure legend, the reader is referred to the web version of this article.)

The overall characteristics of convective motions are also similar among CTRL, R3, and R10. Fig. 18(a) and (b) show the vertical profiles of the root mean square of vertical velocity, $\sqrt{\overline{w^2}}$, averaged only over the active periods and those only over the quiet periods, respectively. The altitudes of the local minimum of $\sqrt{\overline{w^2}}$ generally coincide in all cases for both active and quiet periods. The larger value of $\sqrt{\overline{w^2}}$ during the quiet periods for the case with the stronger cooling indicates that the contrast between the active and the quiet periods becomes less distinct as the increase of body cooling rate.

The period of intermittency is expected to be inversely proportional to the cooling rate if factors other than Q_{rad} in Eq. (14) do not vary. The observed dependence is generally consistent with the expectation above, within a relative error of factor 2, as summarized in Table 2. One reason for the imperfection is that the duration of the active periods becomes non-negligible, since the duration of the quiet periods decreases as Q_{rad} increases. When the length of the active periods, which is typically 1–2 days, is considered, the correspondence between the periods estimated by Eq. (14) and those observed in the model slightly improves, especially in the cases of strong body cooling. Another reason is that the amplitude of the sawtooth-like temperature variation, $\overline{\Delta T}$, moderately depends on the intensity of body cooling; the amplitudes in R3 and R10 is about 1.03 times and 1.5 times as large as that in CTRL, respectively.

References

Anders, E., Grevesse, N., 1989. Abundances of the elements: Meteoritic and solar. Geochim. Cosmochim. Acta 53, 197–214.
Atreya, S.K., Romani, P.N., 1985. Photochemistry and clouds of Jupiter, Saturn and Uranus. Recent Advances in Planetary Meteorology, vol. 17–68. Cambridge Univ. Press, London.
Atreya, S.K., Wong, M.H., Owen, T.C., Mahaffy, P.R., Neimann, H.B., de Pater, I., Drossart, P., Encrenaz, T., 1999. A comparison of the atmosphere of Jupiter and Saturn: Deep atmospheric composition, cloud structure, vertical mixing and origin. Planet. Space Sci. 47, 1243–1262.
Carlson, B.E., Rossow, W.B., Orton, G.S., 1988. Cloud microphysics of the giant planets. J. Atmos. Sci. 45, 2066–2081.
Dyudina, U.A., Del Genio, A.D., Ingersoll, A.P., Porco, C.C., West, R.A., Vasavada, A.R., Barbara, J.M., 2004. Lightning on Jupiter observed in the H-alpha line by the Cassini imaging science subsystem. Icarus 172, 24–36.
de Pater, I., Dunn, D., Romani, P., Zahnle, K., 2001. Reconciling Galileo probe data and ground-based radio observations of ammonia on Jupiter. Icarus 149, 66–78.
Fischer, G. et al., 2011. A giant thunderstorm on Saturn. Nature 475, 75–77.
Fletcher, L.N., Orton, G.S., Rogers, J.H., Simon-Miller, A.A., de Pater, I., Wong, M.H., Mousis, O., Irwin, P.G.J., Jacquesson, M., Yanamandra-Fisher, P.A., 2011. Jovian temperature and cloud variability during the 2009–2010 fade of the South Equatorial Belt. Icarus 213, 564–580.

Friedson, A.J., 2005. Water, ammonia, and H_2S mixing ratios in Jupiter's five-micron hot spots: A dynamical model. Icarus 177, 1–17.
Gautier, D., Hersant, F., Mousis, O., Lunine, J.I., 2001. Enrichments in volatiles in Jupiter new interpretation of the Galileo measurements. Astrophys. J. 550, L227.
Gibbard, S., Lavy, E.H., Lunine, J.I., 1994. Generation of lightning in Jupiter's water cloud. Nature 378, 592–595.
Gierasch, P.J. et al., 2000. Observation of moist convection in Jupiter's atmosphere. Nature 403, 628–630.
Grevesse, N., Asplund, M., Sauval, A.J., 2007. The solar chemical composition. Space Sci. Rev. 130, 105–114.
Gibson, J., Welch, W.J., de Pater, I., 2005. Accurate jovian radio flux density measurements show ammonia to be subsaturated in the upper troposphere. Icarus 173, 439–446.
Hanel, R.A., Conrath, B.J., Herath, L.W., Kunde, V.G., Pirraglia, J.A., 1981. Albedo, internal heat, and energy balance of Jupiter: Preliminary results of the Voyager infrared investigation. J. Geophys. Res. 86, 8705–8712.
Hersant, F., Gautier, D., Lunine, J.I., 2004. Enrichment in volatiles in the giant planets of the Solar System. Planet. Space Sci. 52, 623–641.
Hueso, R., Sanchez-Lavega, A., 2001. A three-dimensional model of moist convection for the giant planets: The Jupiter case. Icarus 151, 257–274.
Ingersoll, A.P., Kanamori, H., 1995. Waves from the collisions of Comet Shoemaker-Levy 9 with Jupiter. Nature 374, 706–708.
Kessler, E., 1969. On the Distribution and Continuity of Water Substance in Atmospheric Circulation, Meteor. Monogr., 10. American Meteorological Society, Boston.
Klemp, J.B., Wilhelmson, R.B., 1978. The simulation of three-dimensional convective storm dynamics. J. Atmos. Sci. 35, 1070–1096.
Li, L., Ingersoll, A.P., Vasavada, A.R., Porco, C.C., DelGenio, A.D., Ewald, S.P., 2004. Life cycles of spots on Jupiter from Cassini images. Icarus 172, 9–23.
Little, B., Anger, C.D., Ingersoll, A.P., Vasavada, A.R., Senske, D.A., Breneman, H.H., Borucki, W.J., the Galileo SSI Team, 1999. Galileo images of lightning on Jupiter. Icarus 142, 302–323.
Nakajima, K., Matsuno, T., 1988. Numerical experiments concerning the origin of cloud clusters in the tropical atmosphere. J. Meteor. Soc. Japan 66, 309–329.
Nakajima, K., Takehiro, S., Ishiwatari, M., Hayashi, Y.-Y., 2000. Numerical modeling of Jupiter's moist convection layer. Geophys. Res. Lett. 27, 3129–3133.
Palotai, C., Dowling, T.E., 2008. Addition of water and ammonia cloud microphysics to the EPIC model. Icarus 194, 303–326.
Rogers, J.H., 1995. The Giant Planet Jupiter. Cambridge Univ. Press, London.
Rossow, W.B., 1978. Cloud microphysics: Analysis of the clouds of Earth, Venus, Mars, and Jupiter. Icarus 36, 1–50.
Sanchez-Lavega, A. et al., 2008. Depth of a strong jovian jet farm a planetary-scale disturbance driven by storms. Nature 451, 437–440.
Showman, A.P., Dowling, T.E., 2000. Nonlinear simulations of Jupiter's 5-micron hot spots. Science 289, 1737–1740.
Showman, A.P., de Pater, I., 2005. Dynamical implication of Jupiter's tropospheric ammonia abundance. Icarus 174, 192–204.
Simon-Miller, A.A., Conrath, B., Gierasch, P.J., Beebe, R.F., 2000. A detection of water ice on Jupiter with Voyager IRIS. Icarus 145, 454–461.
Sromovsky, L.A. et al., 1998. Galileo probe measurements of thermal and solar radiation fluxes in the jovian atmosphere. J. Geophys. Res. 103, 22929–22978.
Sromovsky, L.A., Fry, P.M., 2010. The source of 3-μm absorption in Jupiter's clouds: Reanalysis of ISO observations using new NH_3 absorption models. Icarus 210, 211–229.
Straka, J.M., 2009. Cloud and Precipitation Microphysics. Cambridge Univ. Press, New York, pp. 392.
Stoker, C.R., 1986. Moist convection: A mechanism for producing the vertical structure of the jovian equatorial plumes. Icarus 67, 106–125.
Sugiyama, K., Odaka, M., Kuramoto, K., Hayashi, Y.-Y., 2006. Static stability of the jovian atmospheres estimated from moist adiabatic profiles. Geophys. Res. Lett. 33, L03201. http://dx.doi.org/10.1029/2005GL024554.
Sugiyama, K., Odaka, M., Nakajima, K., Hayashi, Y.-Y., 2009. Development of a cloud convection model to investigate the Jupiter's atmosphere. Nagare Multimedia (J. Japan Soc. Fluid Mech.). <http://www2.nagare.or.jp/mm/2009/sugiyama/>.
Sugiyama, K. et al., 2011. Intermittent cumulonimbus activity breaking the three-layer cloud structure of Jupiter. Geophys. Res. Lett. 38, L13201. http://dx.doi.org/10.1029/2011GL047878.
Vasavada, A.R., Showman, A.P., 2005. Jovian atmospheric dynamics: An update after Galileo and Cassini. Rep. Prog. Phys. 68, 1935–1996.
Weidenschilling, S.J., Lewis, J.S., 1973. Atmospheric and cloud structure of the jovian planet. Icarus 20, 465–476.
West, R.A., Strobel, D.F., Tomasko, M.G., 1986. Clouds, aerosols, and photochemistry in the jovian atmosphere. Icarus 65, 161–217.
Wong, M.H., Mahaffy, P.R., Atreya, S.K., Niemann, H.B., Owen, T.C., 2004. Updated Galileo probe mass spectrometer measurements of carbon, oxygen, nitrogen, and sulfur on Jupiter. Icarus 171, 153–170.
Yair, Y., Levin, Z., Tzivion, S., 1992. Water-cumulus in Jupiter's atmosphere: Numerical experiments with and axisymmetric cloud model. Icarus 98, 72–81.
Yair, Y., Levin, Z., Tzivion, S., 1995. Microphysical processes and dynamics of a jovian thundercloud. Icarus 114, 278–299.
Yair, Y., Levin, Z., Tzivion, S., 1998. Model interpretation of jovian lightning activity and Galileos probe result. J. Geophys. Res. 103, 14,157–14,166.